Hidden magma system causing intense earthquake swarm in the northeastern Noto Peninsula, Japan

Keisuke Yoshida[1], Masaoki Uno[1], Toru Matsuzawa[1], Yohei Yukutake[2], Yusuke mukuhira[1], Hiroshi Sato[3], and Takeyoshi Yoshida[4]

[1]Tohoku University
[2]Earthquake Research Institute
[3]Earthquake Research Institute, The University of Tokyo, Tokyo, Japan
[4]Tohoku University - Graduate School of Science

December 7, 2022

Abstract

An intense earthquake swarm is occurring in the crust of the northeastern Noto Peninsula, Japan. Fluid movement related to volcanic activity is often involved in earthquake swarms in the crust, but the last volcanic activity in this area occurred in the middle Miocene (15.6 Ma), and no volcanic activity has occurred since then. In this study, we investigated the cause of this earthquake swarm using spatiotemporal variation of earthquake hypocenters and seismic reflectors. Hypocenter relocation revealed that earthquakes moved from deep to shallow areas via many planes, similar to earthquake swarms in volcanic regions. The strongest M5.4 earthquake initiated near the migration front of the hypocenters. Moreover, it ruptured the seismic gap between the two different clusters. The initiation of this earthquake swarm occurred at a locally deep depth (z = ~17 km), and we found a distinctive S-wave reflector, suggesting a fluid source in the immediate vicinity. The local hypocenter distribution revealed a characteristic ring-like structure similar to the ring dike that forms just above the magma reservoir and is associated with caldera collapse and/or magma intrusion. These observations suggest that the current seismic activity was impacted by fluids related to ancient or present hidden magmatic activity, although no volcanic activity was reported. Significant crustal deformation was observed during this earthquake swarm, which may also be related to fluid movement and contribute to earthquake occurrences. A seismic gap zone in the center of the swarm region may represent an area with aseismic deformation.

Hosted file

`essoar.10512876.1.docx` available at https://authorea.com/users/533568/articles/611082-hidden-magma-system-causing-intense-earthquake-swarm-in-the-northeastern-noto-peninsula-japan

Posted on 7 Dec 2022 — CC-BY 4.0 — https://doi.org/10.1002/essoar.10512876.1 — This a preprint and has not been peer reviewed. Data may be preliminary.

Hidden magma system causing intense earthquake swarm in the northeastern Noto Peninsula, Japan

Keisuke Yoshida[1,*], Masaoki Uno[2], Toru Matsuzawa[1], Yohei Yukutake[3], Yusuke Mukuhira[4], Hiroshi Sato[3], Takeyoshi Yoshida[5]

[1] Research Center for Prediction of Earthquakes and Volcanic Eruptions, Graduate School of Science, Tohoku University, Sendai, Japan

[2] Graduate School of Environmental Studies, Tohoku University, Sendai, Japan

[3] Earthquake Research Institute, The University of Tokyo, Tokyo, Japan.

[4] Institute of Fluid Science, Tohoku University, Sendai, Japan

[5] Department of Earth Science, Tohoku University, Sendai, Japan

*Corresponding author: Keisuke Yoshida, Research Center for Prediction of Earthquakes and Volcanic Eruptions, Tohoku University, 6-6 Aza-Aoba, Aramaki, Aoba-Ku, Sendai, 980-8578, Japan (`keisuke.yoshida.d7@tohoku.ac.jp`)

Key Points (<140 characters)

1. An intense seismic swarm occurs in a non-volcanic region with hypocenters migrating from deep to shallow depths via many planes.
2. A deep S-wave reflector, suggesting a fluid source, is located near the seismicity initiation point and above the low-velocity anomaly.
3. A ring-fault near the reflector represents part of a hidden, ancient, or new magmatic system that caused the swarm by supplying fluids.

Abstract (243 words < 250)

An intense earthquake swarm is occurring in the crust of the northeastern Noto Peninsula, Japan. Fluid movement related to volcanic activity is often involved in earthquake swarms in the crust, but the last volcanic activity in this area occurred in the middle Miocene (15.6 Ma), and no volcanic activity has occurred since then. In this study, we investigated the cause of this earthquake swarm using spatiotemporal variation of earthquake hypocenters and seismic reflectors. Hypocenter relocation revealed that earthquakes moved from deep to shallow areas via many planes, similar to earthquake swarms in volcanic regions. The strongest M5.4 earthquake initiated near the migration front of the hypocenters. Moreover, it ruptured the seismic gap between the two different clusters. The initiation of this earthquake swarm occurred at a locally deep depth (z = ~17 km), and we found a distinctive S-wave reflector, suggesting a fluid source in the immediate vicinity. The local hypocenter distribution revealed a characteristic ring-like structure similar to the ring dike that forms just above the magma reservoir and is associated with caldera collapse and/or magma intrusion. These observations suggest that the current seismic activity was impacted by fluids related to ancient or present hidden magmatic activity, although no volcanic activity was reported. Significant crustal deformation was observed during this

earthquake swarm, which may also be related to fluid movement and contribute to earthquake occurrences. A seismic gap zone in the center of the swarm region may represent an area with aseismic deformation.

Plain language summary (199 words < 200)

An intense earthquake swarm is currently occurring in the crust of the northeastern Noto Peninsula, Japan. Fluid movement related to volcanic activity is often involved in earthquake swarms in the crust, but no volcanic activity has occurred in this region since the middle Miocene (15.6 Ma). We here investigated the cause of this earthquake swarm using the precisely-determined earthquake locations and seismic reflectors. We found that the earthquakes moved from deep to shallow areas via many planes, similar to seismicity induced by fluid-injection. The strongest M5.4 earthquake initiated near the upward migration front on the largest planar structure. Further earthquakes may be possible in the shallow part of this fault. We found a distinctive S-wave reflector, suggesting a fluid source, in the immediate vicinity of the initiation point of this swarm. The local hypocenters show a characteristic ring-like structure similar to the ring dike that forms above the magma reservoir. These observations suggest that the current seismic activity is being impacted by fluids related to ancient or new hidden magmatic activity. The present results suggest that hidden magma-induced structures and fluids can generate earthquakes even in areas where no volcanic activity has been observed for over 10 million years.

1. Introduction

In subduction zones, fluids ascending from subducting oceanic slabs play an essential role in various tectonic processes, such as magmatic activity, formation of volcanic and lithospheric structures, and generation of crustal earthquakes, in the overriding plane (Hasegawa et al., 2005; Iwamori, 1998; Mcbirney, 1969; Tatsumi et al., 1983). The magma that ascends from the depths does not necessarily erupt but may remain underground and solidify gradually. During the solidification process, magma chambers trapped within the crust provide fluid to the interior of the crust, which may affect the occurrence of crustal earthquakes (Hasegawa et al., 2005).

Crustal earthquakes in subduction zones often occur around volcanoes. Examples include the 2008 M7 Iwate–Miyagi Nairiku earthquake (Yoshida et al., 2014), earthquake swarms in Hakone (Yukutake et al., 2010) and Moriyoshi (Kosuga, 2014) in Japan, those in the Yellowstone (Shelly et al., 2013) and Mammoth Mountain (Shelly & Hill, 2011) in the USA, and those in the West Bohemia/Vogtland region (Fischer et al., 2014). Previous studies have suggested that deep crustal fluids related to magmatic activity reduce the strength of the fault and cause earthquakes. Earthquake swarms, in particular, often exhibit migration behaviors of hypocenters similar to fluid-injection-induced seismicity (Cox, 2016; Kosuga, 2014; Parotidis et al., 2003; Shelly et al., 2013; Yukutake et al., 2010), supporting the contribution of fluid movement and possible aseismic slips for their occurrence. Seismic low-velocity zones and seismic reflectors are

often found beneath the seismogenic zone, suggesting that fluids are concentrated near the reflectors (Hori et al., 2004; Taira et al., 2007; Umino et al., 2002).

Earthquakes also frequently occur near paleo-volcanoes and paleo-calderas where volcanic activity has ceased in the past (more than a million years ago). For example, in Japan, intense earthquake swarms recently occurred near paleo-calderas at the Yamagata–Fukushima border area (Okada et al., 2015; Yoshida et al., 2016), Sendai–Okura area (Yoshida & Hasegawa, 2018b), and Kagoshima Bay area (Matsumoto et al., 2021). These earthquakes show similar characteristics to earthquake swarms in active volcanic regions, including hypocenter migration from deep to shallow areas and the presence of low-velocity regions and seismic reflectors beneath the source region (Kosuga, 2014; Okada et al., 2015; Yoshida et al., 2016; Yoshida & Hasegawa, 2018a and b; Matsumoto et al. 2021). These similarities suggest that the occurrence of earthquake swarms around paleo-calderas is also related to fluid behavior. The source of such fluid is considered to be an old (several Ma), almost solidified magma chamber.

Crustal earthquakes in subduction zones, however, also occur in areas apart from known volcanoes and paleo-calderas. Even in the case of these earthquakes, crustal fluids of slab origin may be involved as such fluids do not necessarily correlate with volcanic activity. In some fore-arc regions of the volcanic front (such as the Kii Peninsula and the Arima Onsen area in Japan), fluids originating from the slab ascend directly near the surface without magma formation (Kusuda et al., 2014; Morikawa et al., 2016). Deep low-frequency earthquakes, a phenomenon related to fluids, are often observed near volcanoes in the plate (Hasegawa & Yamamoto, 1994) and sometimes occur in areas far from the volcanoes (Aso et al., 2011), which is consistent with the idea that deep fluids are distributed outside the immediate vicinity of the volcano or paleo-caldera. However, the degree of fluid involvement in crustal earthquakes in subduction zones is not well understood.

Since December 2020, an intense earthquake swarm has occurred in the northeastern Noto Peninsula (Fig. 1) in Japan, which is an example of crustal earthquakes far from volcanoes and paleo-calderas. The area is marked by thick (2 km+) Oligocene to middle Miocene volcanic and volcaniclastic rocks that erupted in the pre- to syn-opening stage of the Japan Sea (Yoshikawa et al., 2002). Surface geological studies revealed that volcanic activity terminated at ca. 14 Ma and the area is covered by marine sediments. Because of the shortening deformation since the latest Miocene, ENE–WSW trending folds and reverse faults have developed in this area (Yoshikawa et al., 2002; Ozaki, 2010). Along the northern coast of the Noto Peninsula, active marine faults run parallel to the coastline (Inoue and Okamura, 2010).

The occurrence mechanism of the current earthquake swarm is essential for evaluating the future development of seismicity. An active fault segment (Suzuoki segment) exists immediately north of this swarm area (black thick line in

Fig. 1a; Inoue et al., 2010). This earthquake swarm continues to be active as of October 2022, and the largest earthquake to date was the M5.4 earthquake that occurred on June 19, 2022. In the surrounding area, an M6.6 earthquake occurred in 1993, just north of the current earthquake swarm (Fig. 1a), and an M6.6–7 earthquake occurred in 1729 (Usami, 2003). In 2007, an M6.9 earthquake and its aftershocks occurred in an area far-west (Kato et al., 2008). Whether the present earthquake swarm will lead to a large earthquake is an important question. In this study, we investigated the occurrence mechanism of this earthquake swarm based on its commonalities with fluid-related earthquake swarms. In particular, we examined earthquake migration and the presence of deep seismic reflectors and low-velocity areas. Based on this, we suggested the possibility that this current activity is caused by fluid movements related to a hidden magmatic structure.

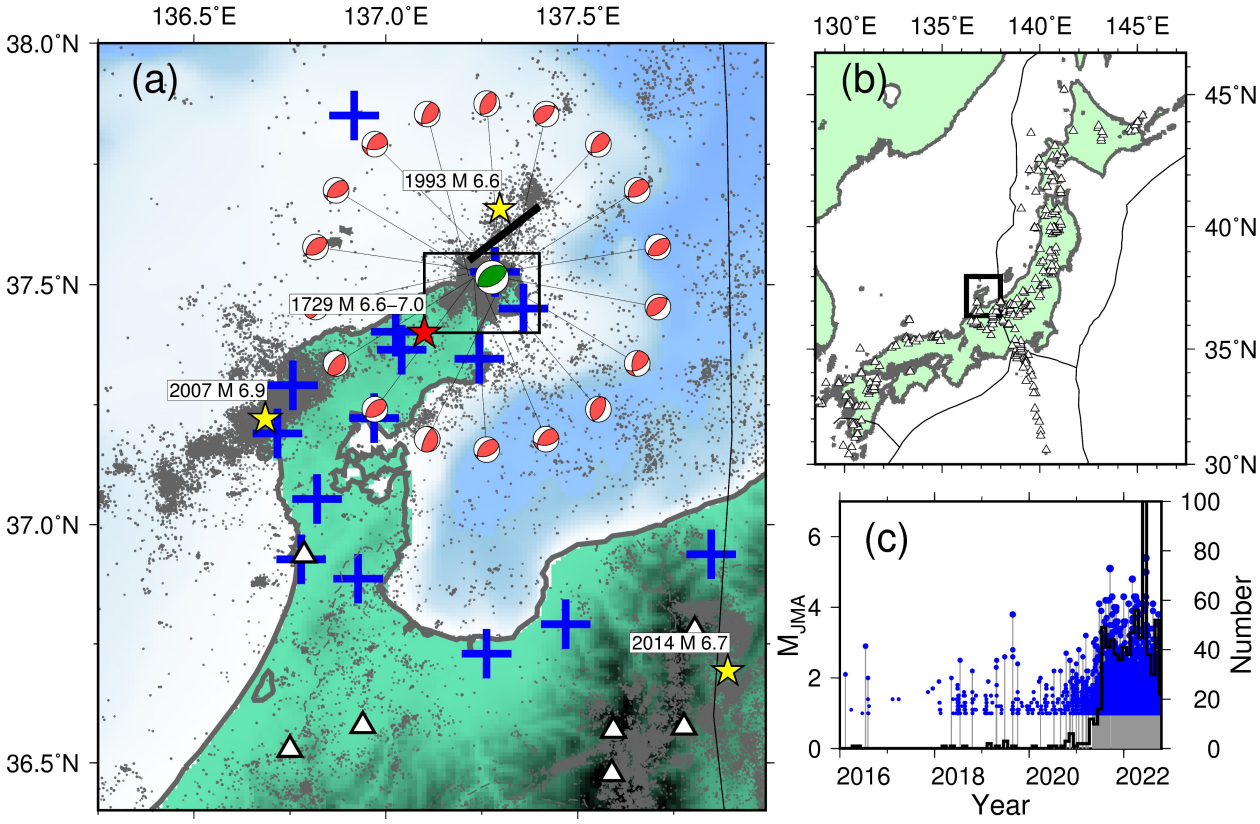

Figure 1. (a) Map showing the location of the study region. The rectangle indicates the study area, and triangles indicate Quaternary volcanoes. The thick black line represents the Suzu-oki active fault segment (Inoue et al., 2010). Gray dots show the hypocenters of shallow earthquakes (z < 40 km) with the JMA magnitude $M_{\mathrm{JMA}} \geq 2.0$ for the period from January 1, 2003, to September 30, 2022. Yellow stars indicate earthquakes of M6.5 that have occurred since 1919.

Red star indicates the ~M7 earthquake in 1929 (Usami, 2003). Beach ball shows the moment tensor solution by F-net. Green color is the maximum earthquake of M5.4. Blue crosses indicate the distribution of stations in this analysis. (b) Map showing the area of (a) by rectangle. (c) Magnitude–time diagrams of events in the source region of the Northeast Noto swarm. Blue circles with gray bars indicate the earthquake magnitudes in the JMA unified catalog. The black line denotes the number of earthquakes M>2.

2. Fault structure and earthquake migration

We relocated earthquake hypocenters around the source region of the earthquake swarm in the northeastern Noto Peninsula according to previous studies (Yoshida & Hasegawa, 2018a, 2018b). We used the 1-D velocity model of Hasegawa et al. (1978) for relocation. The waveform cross-correlation-based double-difference earthquake relocation method (Waldhauser & Ellsworth, 2000) was applied to 10950 $M_{\mathrm{JMA}} \geq 1$ earthquakes from March 1, 2003 to September 30, 2022 in the Japan Meteorological Agency (JMA) unified catalog (Figs. 1a and S1). This process was essentially the same as that described by Yoshida and Hasegawa (2018a, 2018b). Waveform data were derived from the JMA and Hi-net (NIED, 2019b) and F-net (NIED, 2019a) of the National Research Institute for Earth Science and Disaster Resilience (NIED) (Fig. 1).

We used 280,915 P-wave and 282,817 S-wave differential arrival time data derived from the arrival time data in the JMA unified catalog. We also used 26,545,802 P-waves and 19,922,017 S-wave differential arrival time data derived from the waveform correlation analysis. Figure 2b shows the relocated locations of the 10940 events. Almost all of the 10950 events were relocated with the DD algorithm. The location data for ten earthquakes were removed because their hypocenters were located above the ground surface or contained outliers in the differential arrival time data. The uncertainty in earthquake locations was evaluated via 100 bootstrap resamplings of the differential arrival time data. Median lengths of the 95% confidence intervals were 0.0023° in longitude, 0.0021° in latitude, and 0.37 km in depth.

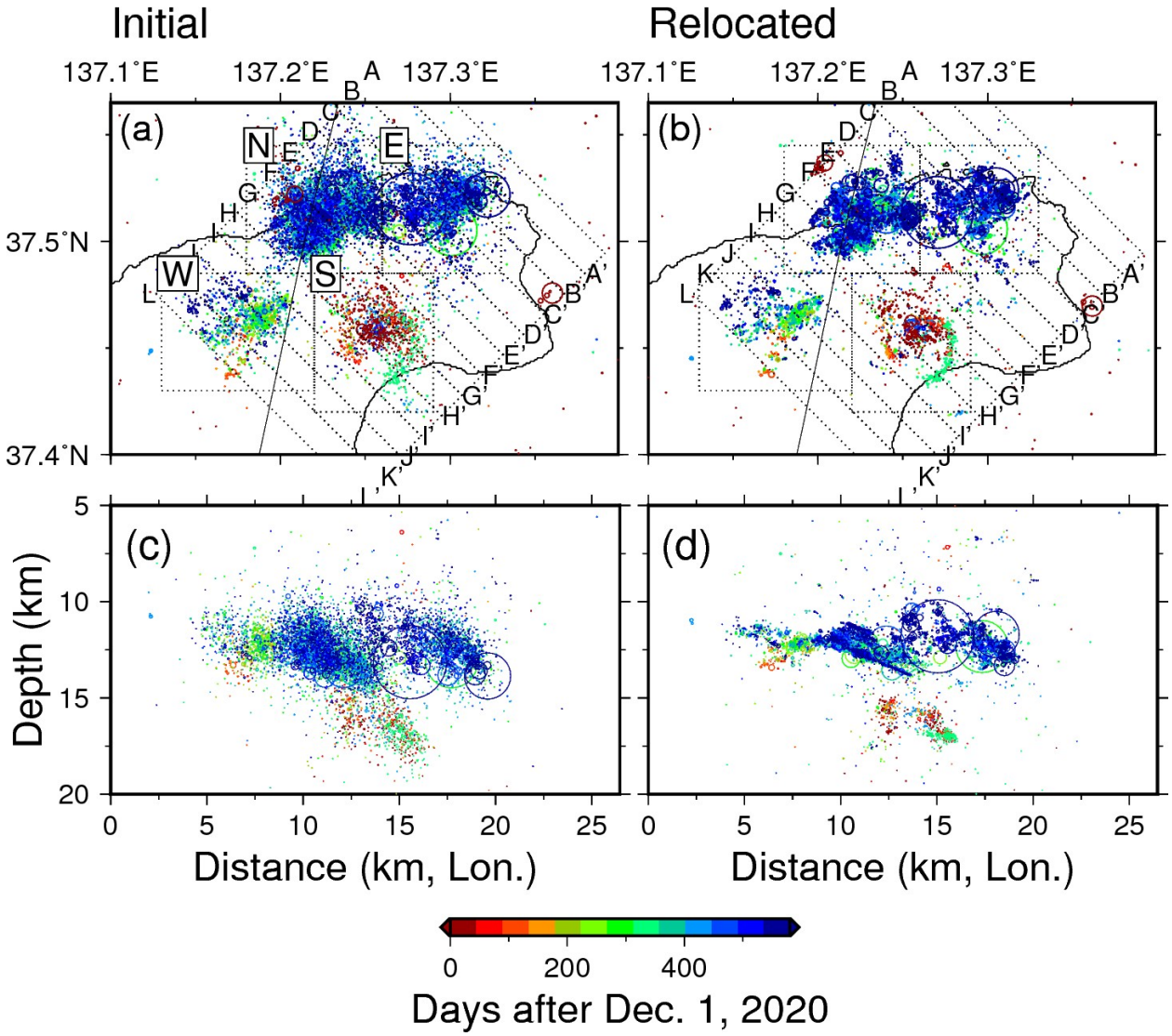

Figure 2. Hypocenter distributions. (a), (c): the original hypocenters listed in the JMA unified catalog. (b), (d): the relocated hypocenters in this study. (a) and (b) show the map view, and (c) and (d) show the cross-sectional view along the longitude direction. The sizes of the circles correspond to the fault diameter, assuming a stress drop of 10 MPa. The color scale shows the occurrence time of each earthquake. Dotted squares represent four clusters.

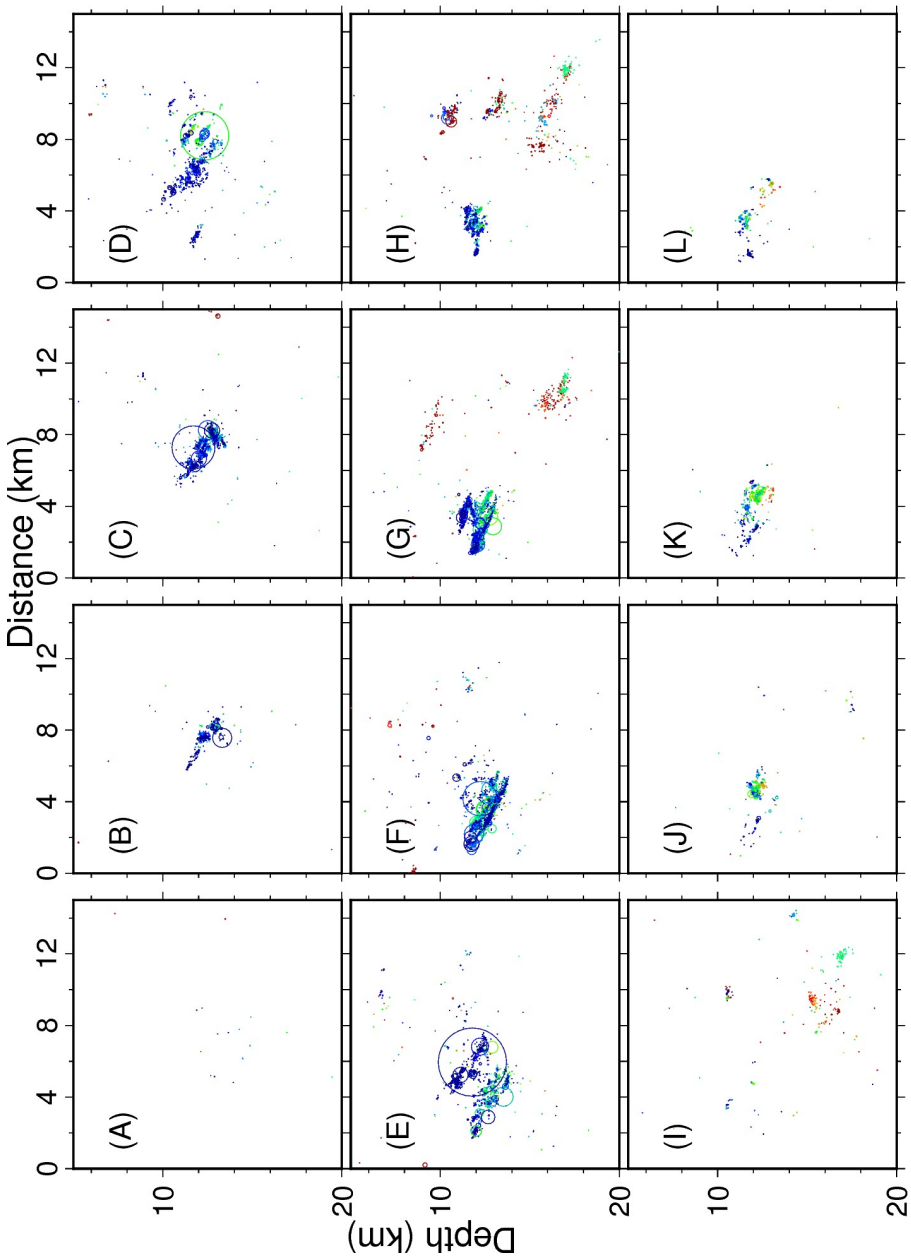

Figure 3. Cross-sectional view of the relocated hypocenters. The 12 figures show across-fault vertical cross-sections along the lines shown in Figure 2. The color scale denotes the occurrence time of each earthquake.

Comparison of Figures 2a and 2b shows that our relocation allowed a much finer view of the fault structure. The source area can be roughly divided into four

clusters, referred to as clusters S, W, N, and E, as shown in Figure 2. The effect of hypocenter relocation was more pronounced in the depth direction than in the horizontal direction as shown in Figures S1 and 3, which show a cross-section of the entire area before and after relocation in the northwest–southeast direction, which is normal to the predominant strike direction of the focal mechanisms (Fig. 1). The hypocenters that appeared cloud-like and scattered before relocation (Fig. S1) were concentrated in many planar structures.

Most earthquakes occur at depths below 14 km. However, cluster S had a significantly deeper depth limit for earthquakes, with earthquakes occurring as deep as z = 18 km. In this cluster, earthquakes occurred at three depths of approximately 17, 13, and 10 km (Figs. 3H and S2). Figures 4 and 5 show the hypocenter locations in the map and cross-sectional views for 16 different periods (measured from December 1, 2020). A cluster of earthquakes at a depth of ~17 km occurred at the beginning of this earthquake sequence (Figs. 4a and 5a). Seismic activity started in Cluster S and became more active in the order of Clusters W, N, and E.

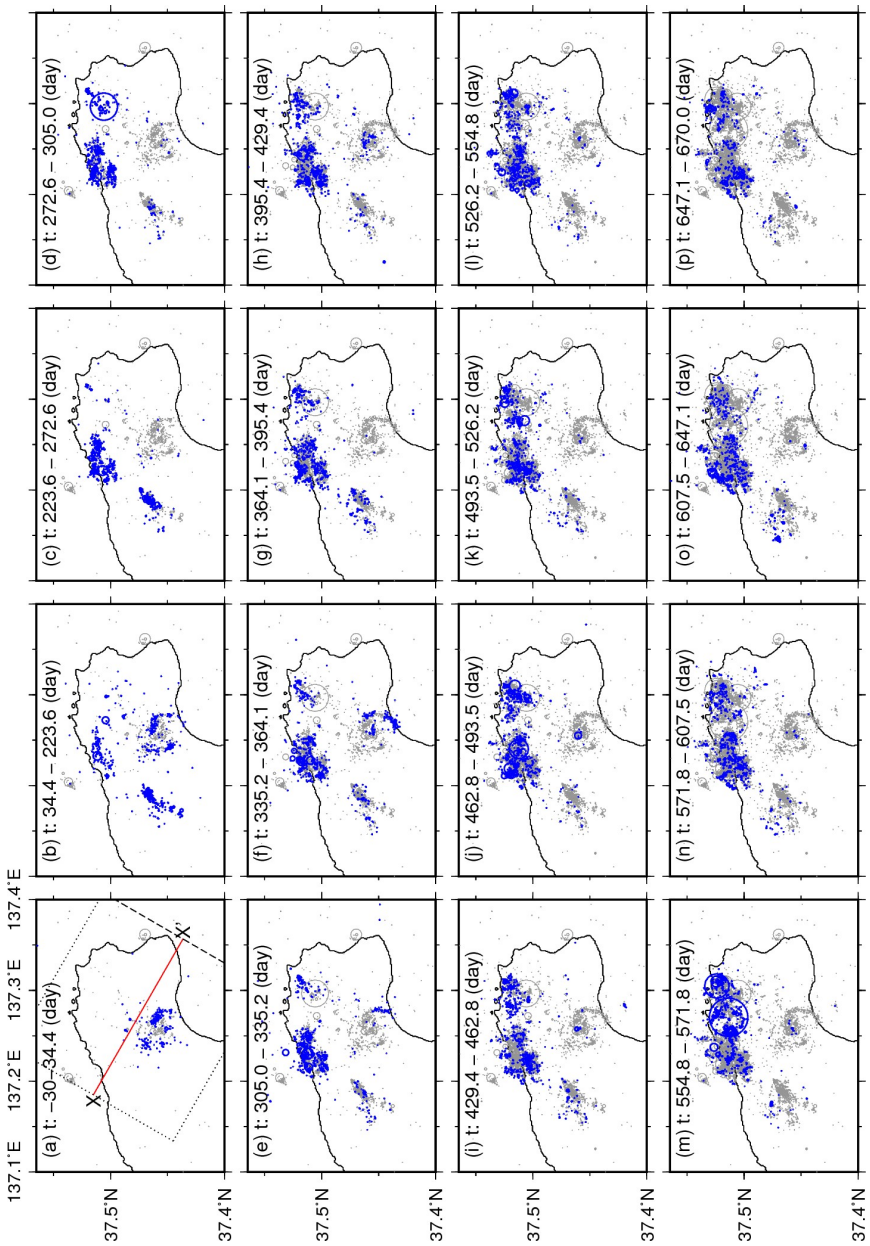

Figure 4. Earthquake locations in each time window. Time t is measured from December 1, 2020. Blue circles indicate the earthquake hypocenters within the time window, and gray circles indicate the locations of earlier earthquakes. The lines and squares in (a) represent the locations of the cross sections in Figure 5.

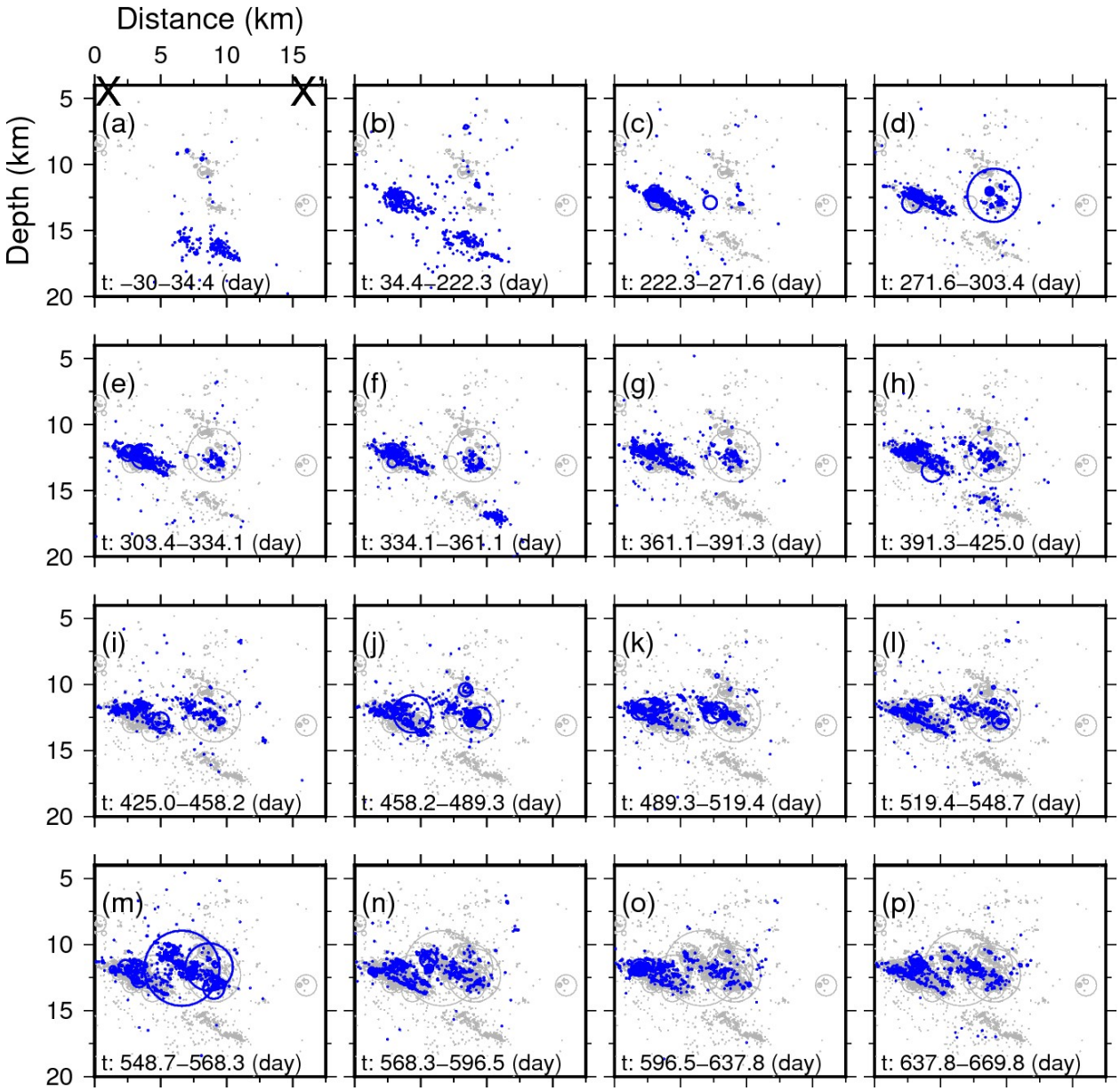

Figure 5. Cross-sectional view of the earthquake hypocenters in each time window. Time t is measured from December 1, 2020. The orientation of the cross sections is shown in Figure 4a. Blue circles indicate the locations of earthquakes within the time window, and gray circles indicate the locations of earlier earthquakes.

Figure 5 shows that the depth of the earthquake gradually expanded in a shal-

lower direction via many planes. Figure 6 directly compares the timings and depths of the earthquakes for the entire source region and each cluster. The depth of the earthquakes gradually expanded toward the shallow side in each of the three clusters x (Figs. 6d–f). except for Cluster S (Fig. 6c), wherein the earthquakes were intermittent and complex.

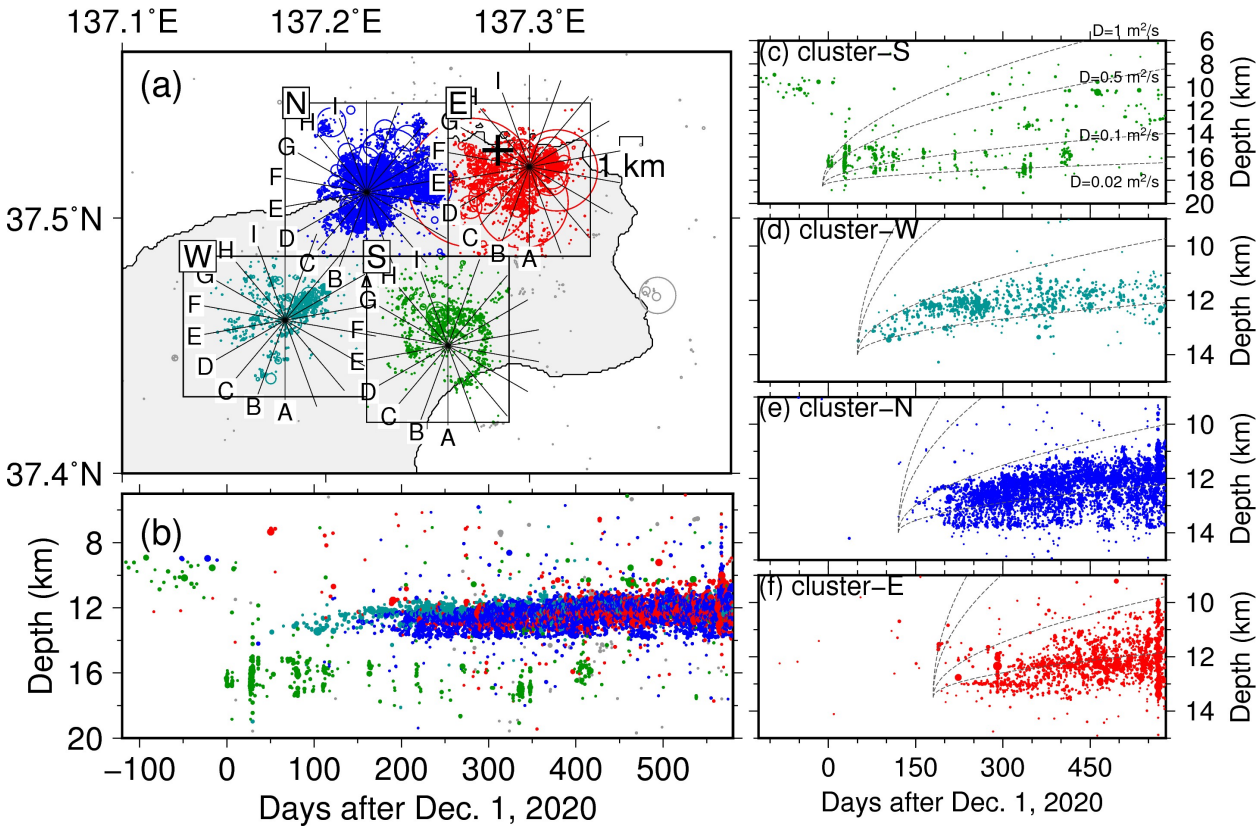

Figure 6. Temporal changes in earthquake depth. Four different colors represent the four clusters. (a) Map showing the earthquakes in the four clusters. (b) Comparison of time and earthquake depth. (c)–(f) Comparisons of time and earthquake depth for each cluster. The contours show the diffusion front for diffusion coefficients of $D = 0.02,\ 0.1,\ 0.5$, and $1.0\ \mathrm{m}^2/s$.

Figure 7 shows a cross-section of earthquakes in the northern clusters (N, E) concentrated on well-defined fault structures (Figs. 3, S4, S5). The earthquakes occurred on several parallel planes dipping in the east–southeast direction. The largest M5.4 earthquake also occurred on one of the east–southeast dipping planes in the region between Clusters N and E (Fig. 7e). A small number of planes were nearly conjugated to the east–southeast dipping planes and appeared to be connected to the east–southeast dipping planes (Fig. 7g, h). Figure 7 indicates the order of earthquake occurrence by color, showing that the move-

ment of the earthquake hypocenters from shallow to deep occurred via multiple planar structures. Video S1 shows the temporal variations in the hypocenters of the entire source area. Some earthquakes moved from shallow to deep along the planar structures, but overall, the earthquake locations moved from deep to shallow, which is consistent with Figure 6.

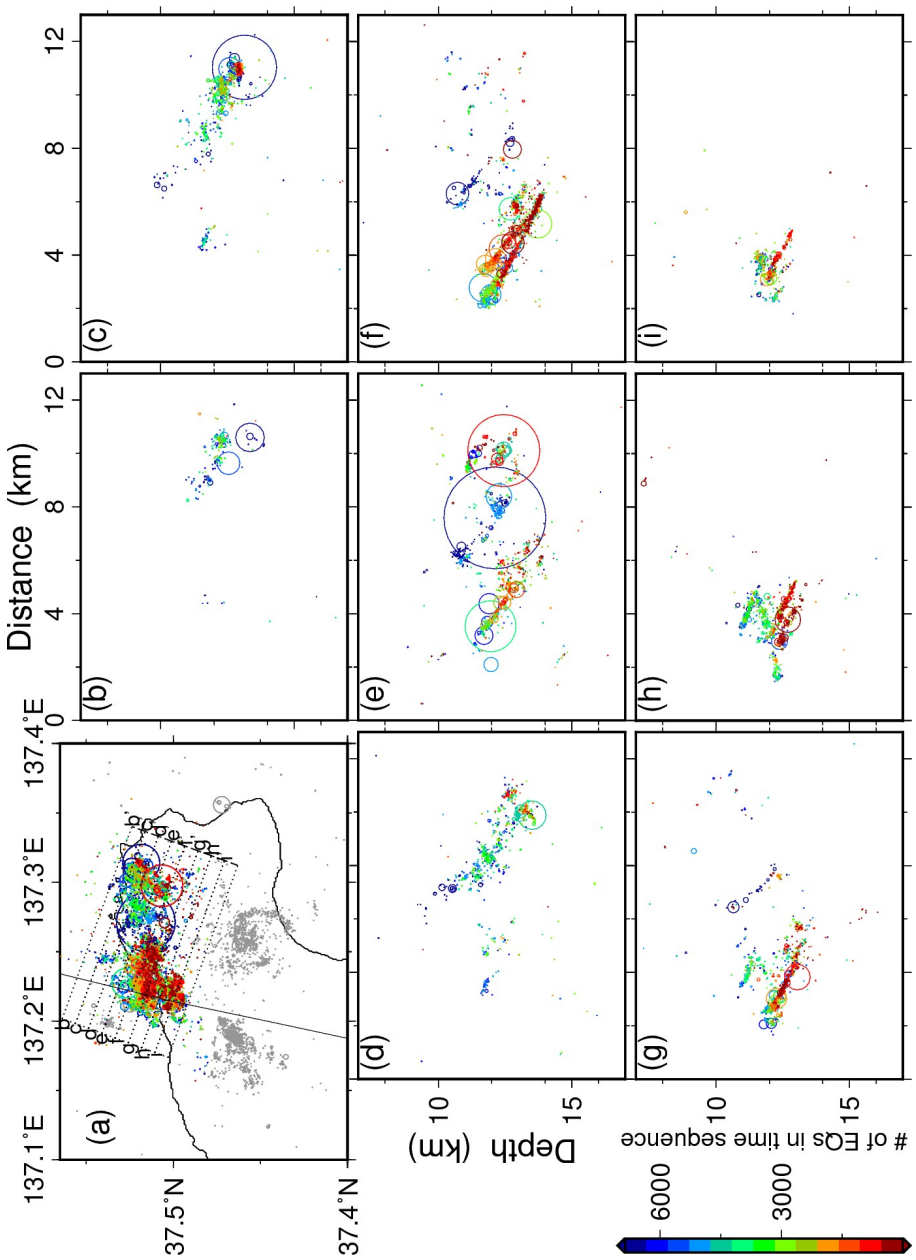

Figure 7. Distribution of the relocated hypocenters in the northern part. The color scale shows the relative occurrence time of each earthquake.

The observed earthquake migration was similar to that frequently observed in fluid-injection-induced seismicity (Shapiro et al., 1997) and natural crustal earthquake swarms (Yukutake et al., 2010; Shelly et al., 2013; Kosuga, 2014; Amezawa et al., 2021). In Figure 6, we have also plotted the pore-pressure front based on the fluid diffusion model $r = \sqrt{4\pi Dt}$ using the equation proposed by Shapiro et al. (1997), where D is the hydraulic diffusivity. Here, we only considered migration in the depth direction by assuming that fluid diffusion begins near the initiation point of each cluster. The migration of this earthquake can be roughly explained by a diffusion coefficient of approximately $D = 0.02 - 0.1\ m^2/s$ in Clusters W, N, and E, which is similar to the values observed for earthquake swarms near volcanoes and calderas in the crust of Japan (Yukutake et al., 2010; Kosuga, 2014; Okada et al., 2015; Yoshida & Hasegawa, 2018a and b; Matsumoto et al. 2021; Amezawa et al. 2021). Only in Cluster S, where the depth of earthquake occurrence was divided into several clusters, the migration speed appeared to be fast and was consistent with the curve for approximately $D = 0.5 - 1.0\ m^2/s$. However, some shallow earthquakes occurred in this cluster before the current activity (Fig. 6). The actual patterns of hypocenter movement were complex (Fig. 7) compared to the simple model with a constant diffusion coefficient.

The obtained features were remarkably similar to those observed in earthquake swarms that became active near volcanoes or paleo-caldera in northeastern Japan after the 2011 M9 Tohoku earthquake. Indeed, these earthquake swarms share a marked tendency for earthquake locations to move from deep to shallow using multiple planes, which can be explained by fluid migration (Kosuga, 2014; Yoshida & Hasegawa, 2018a and b; Yoshida et al., 2019) and were inferred to have been caused by fluid movement associated with the crustal deformation of the Tohoku earthquake, despite the decreased shear stress caused by the Tohoku earthquake (Terakawa et al., 2013; Yoshida et al., 2016). The similarity of the migration characteristics of the earthquake swarm in the northeastern Noto Peninsula and the above earthquake swarms suggests that the present activity was also influenced by upward fluid movement.

3. Fault zone of the largest M5.4 earthquake

Figures 8 and 9 show the temporal variation in earthquake locations before and after the largest M5.4 earthquake. Clusters N and E showed a trend of gradual northward expansion of the source area (Figure 8b–c). Until the largest M5.4 earthquake, Clusters N and E were split into two, with only a few earthquakes in the vicinity of the M5.4 hypocenter until approximately 100 days before the earthquake. Many earthquakes occurred within 0.5 km from the planar structure corresponding to the fault plane of the M5.4 earthquake (dark color in Figs. 8a and e). This planar structure extends to the eastern edge of Cluster E, and Cluster E gradually expands westward to the hypocenter of the M5.4 earthquake before the M5.4 earthquake (Fig. 8d). Several M>3 earthquakes occurred in the

vicinity approximately 100 days before the M5.4 earthquake on the same planar structure (blue stars). The M5.4 earthquake finally occurred near the migration front of the previous small earthquakes, and after this earthquake, earthquakes began to occur at shallower depths. Overall, the earthquakes moved from deeper to shallower levels in this planar structure (Fig. 9). This earthquake migration may represent fluid diffusion through a fault zone or aseismic slip propagation.

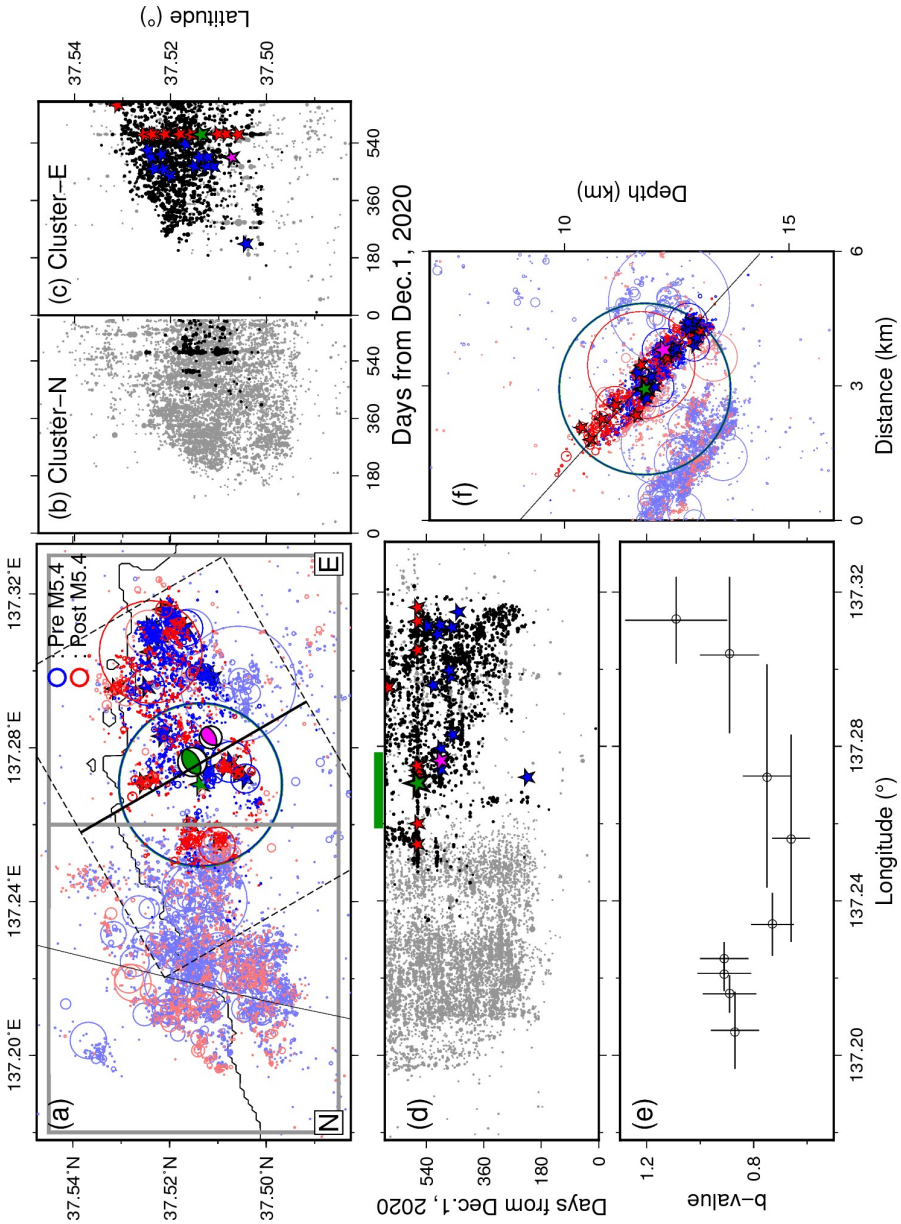

Figure 8. Spatiotemporal variation of the earthquake hypocenters in the northern region where the largest earthquake occurred. (a) and (f) are map and cross-sectional views, respectively, with blue circles indicating the earthquakes before the M5.4 earthquake and red circles indicating the earthquakes after the M5.4 earthquake. Green symbol represents the M5.4 earthquake. Darker colors indicate earthquakes near the M5.4 fault zone (<0.5 km). Stars represent M>3 earthquakes in the area squared in (a). The yellow and pink beach balls in (a) represent the focal mechanisms for the M5.4 and empirical Green's function (EGF) earthquakes. The location and range of the cross-section in (f) are represented by the black line with a dashed rectangle in (a). (b)–(d) represent the relationship between the timings of earthquake occurrence and latitude (b, c) and longitude (d). The green horizontal line indicates the rupture area of the M5.4 earthquake in Figure 9. (e) shows the b-value and standard error (vertical line). Horizontal lines indicate the range of data.

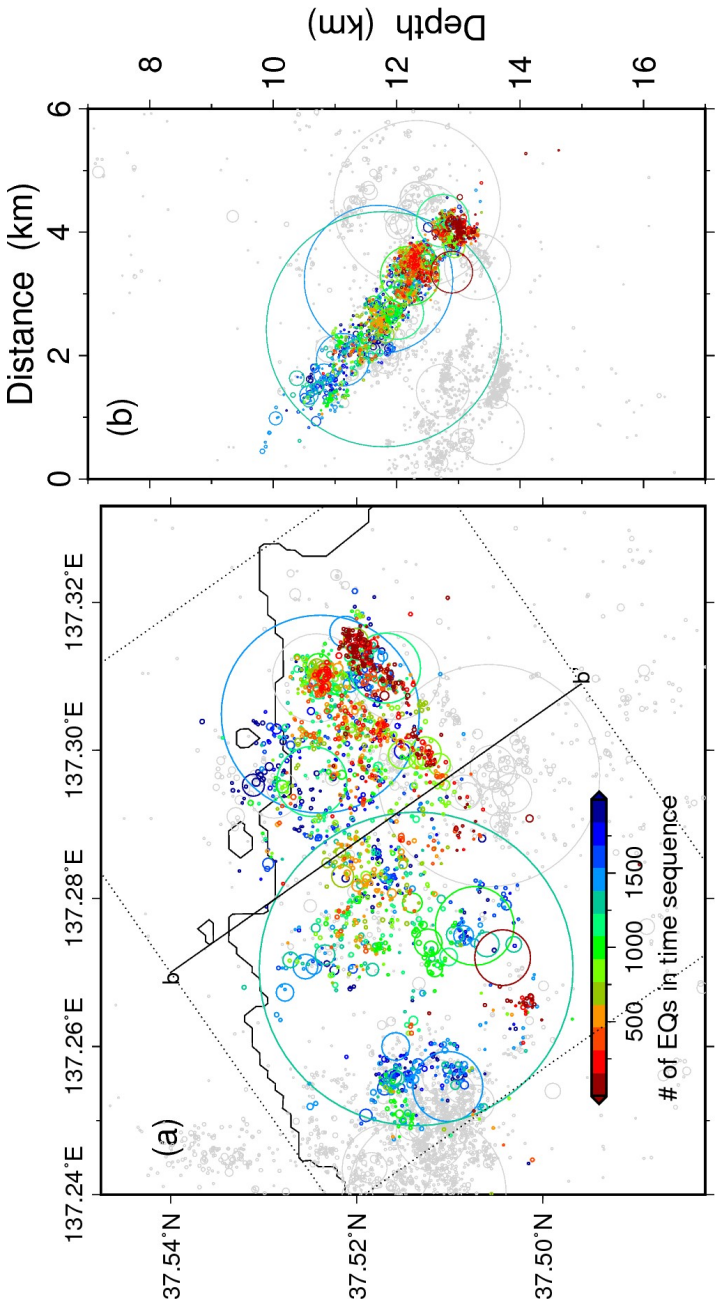

Figure 9. Spatiotemporal variation of the earthquake hypocenters near the fault zone of the M5.4 earthquake within 0.5 km. The color scale shows the relative occurrence time of each earthquake. Gray indicates earthquakes outside the fault zone (> 0.5 km).

To estimate the rupture area of the largest M5.4 (Mw5.2) earthquake, we followed the procedure used by Yoshida et al. (2020) and (2022). We first estimated the apparent moment rate functions (AMRFs) of the M5.4 event by waveform deconvolution and then inverted the AMRFs to obtain the spatiotemporal distributions of the coseismic slips.

We estimated AMRFs using the time–domain deconvolution method of Ligorria & Ammon (1999), which employs the method of Kikuchi & Kanamori (1982), with a non-negative constraint. We selected the waveforms (transverse components of S-waves) of the April 2022 M4.1 earthquake (shown by the pink focal mechanism in Fig. 8) as the empirical Green's functions (EGFs) because it occurred close to the target earthquakes and had a similar focal mechanism to the target M5.4 event and sufficient signal-to-noise ratio. Because the magnitudes of the target and EGF earthquakes are relatively similar, the frequency band should be relatively narrow. We set the cutoff frequency of the low-pass (fourth-order Butterworth-type) filter used in the deconvolution to 2.0 Hz. We used the velocity waveform data from the NIED F-net (NIED, 2019b) and acceleration waveform data from the NIED KiK-net (NIED, 2019c). We used AMRF in further analysis only when a derived AMRF explained more than 80% of the observed waveforms in variance reduction. We derived 17 AMRFs showing clear directional dependence (Figs. 10 and S6); they had large amplitudes and short durations at the western stations and small amplitudes and long durations at the eastern stations. This directional dependence suggests that the M5.4 earthquake rupture propagated westward.

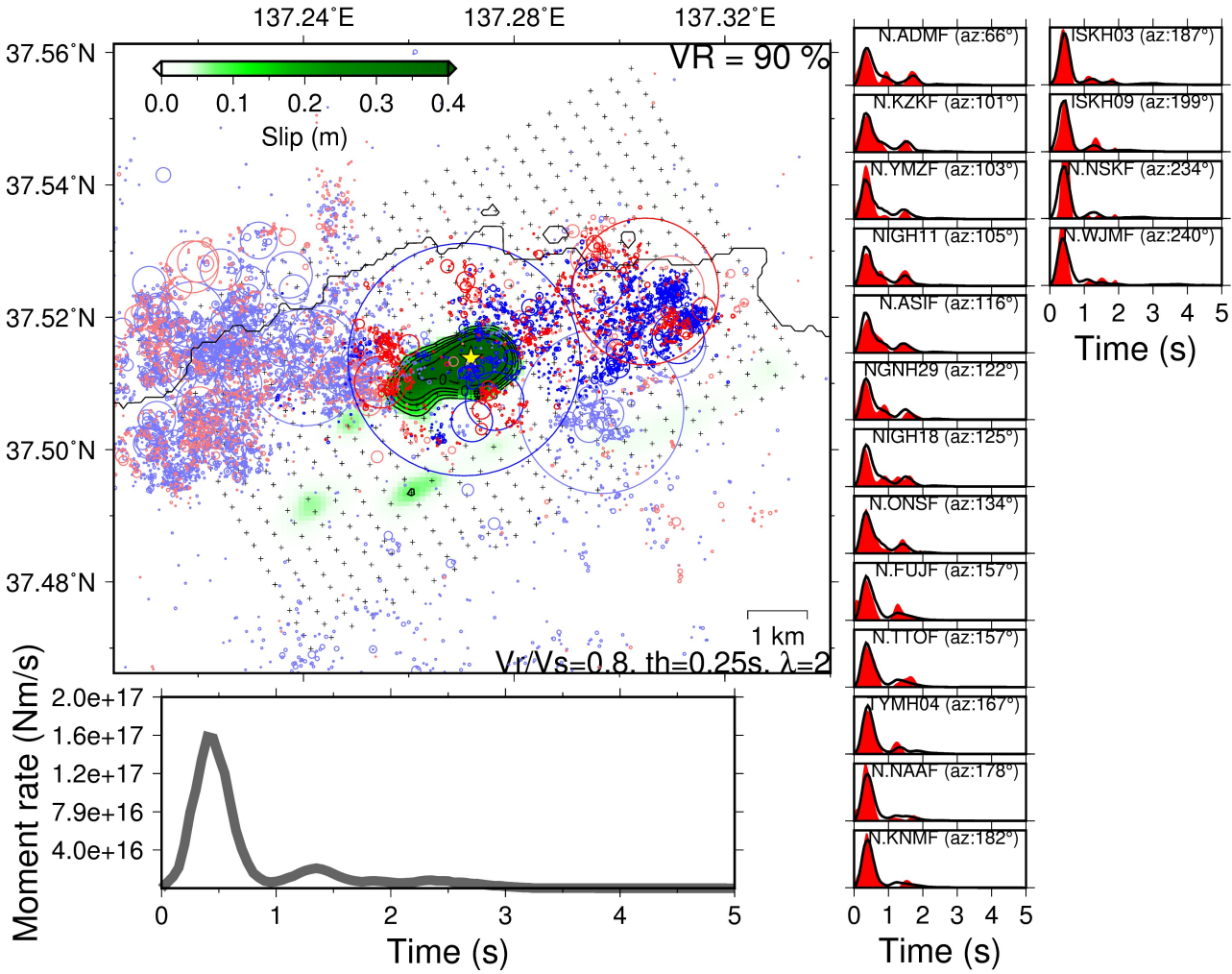

Figure 10. Results of slip inversion of the M5.4 earthquake. (a) Map projection of slip distribution. Blue circles indicate earthquakes before the M5.4 earthquake, and red circles indicate earthquakes after the M5.4 earthquake. Darker colors represent earthquakes on the M5.4 earthquake fault. (b) Source time function. (c) AMRF fitting; red is observation and black is the model result.

We estimated the rupture process and slip distribution of the M5.4 earthquake using the methods of Hartzell & Heaton (1983) and Ross et al. (2018). Because we used relatively low-frequency waveforms (<2.0 Hz) in the inversion, we focused on the macroscopic characteristics (i.e., rupture propagation direction and slip area) rather than the details of the rupture process. The assumptions are as follows: (1) the rupture initiates at the center of a rectangular fault with a strike of 61° and dip angle of 51°, which is consistent with the focal mechanism (Fig. 8a); and (2) the rupture front propagates over the fault with a constant ve-

locity $V_r = 0.8V_s = 2.9\ km/s$. We set the fault length and width to 9.6 km and divided it into 25 × 25 subfaults. We computed the relative delay times between each subfault and station using the 1-D model for hypocenter relocation. The local moment–rate function at each subfault is represented by the superposition of the four triangular submoment rate functions (sMRFs). We determined the half-duration of sMRFs $t_h = 0.25\ s$, considering the cut-off filter of the low-pass filter (2.0 Hz). At each subfault, the first sMRF was aligned when the rupture front reaches the center, and the subsequent sMRFs followed at a regular time interval of t_h. We used the non-negative least-squares algorithm of Lawson & Hanson (1995) to obtain the amplitudes of the sMRFs with a damping factor (λ) and a smoothing factor (e_s). We assumed the same values for λ and e_s and determined the specific values of $\lambda = e_s$ =2 based on a trade-off curve. AMRFs were downsampled at 0.05-s intervals.

The slip distribution obtained from the AMRF inversion reproduced the observed AMRFs well (Fig. 10), with the variance reduction (VR) between the observed and theoretical waveforms being approximately 90%. According to hypocenter information, the rupture began at the western end of the eastern region (Cluster E), where small earthquakes occurred in the deeper part of the fault. Our slip inversion results indicated that the rupture propagated further west, producing a large slip primarily in the gap between Clusters N and E (Figure 8d). The size of the rupture area of the M5.4 earthquake was roughly comparable to that of this gap along the longitudinal direction (Figs. 8d, 10). The aftershocks occurred at the periphery of the rupture zone.

We computed the radiated energy using the source time function with the method of Vassiliou & Kanamori (1982) and obtained the value of $E_R = 2.94 \times 10^{10}$ J, and the scaled energy was $e_R = E_R/M_0 = 3.7 \times 10^{-5}$. Note that our inversion used a triangular sMRF, which extrapolates the high frequencies removed by a low-pass filter with an omega-square envelope (Haskell, 1964). The value of e_R was close to the typical value for earthquakes occurring in the crust of the Japanese Islands (Kanamori et al., 2020).

A difference was noted in the style of earthquake occurrence in the longitudinal direction (Fig. 8a). Figure 8e shows the b-values calculated by dividing the area into longitudinal sections using earthquakes prior to the M5.4 earthquake. The cutoff magnitude was set to 2, and the same number of earthquakes (n = 100) were used for each longitude range. Standard errors were obtained according to the method described by Shi & Bolt (1982). The b-value was slightly less than 1.0 but was in the typical range of values. The b-value was lower in the region between Clusters N and E, where the M5.4 earthquake occurred later, although the variation was approximately the same as the standard deviation and the magnitude–frequency distribution presented a somewhat complex shape in the central region. The unique interpretation of the b-value is difficult, but the obtained result may mean that the differential stress was relatively high in this region before the M5.4 earthquake (Scholz, 1968 and 2015). Alternatively, based on the reported positive relationship between pore pressure (inversely correlated

with fault strength) and b-value (Bachmann et al., 2012; Mukuhira et al., 2021; Yoshida et al., 2017), the results may suggest that the effect of fluid on fault strength reduction was more pronounced in the western and eastern segments and less pronounced in the rupture area of the M5.4 earthquake between the two segments.

4. S-wave reflector and fluid source

Motivated by the deep-to-shallow migration of the earthquake hypocenters described in Section 2, we attempted to detect S-wave reflectors in this region. Previous studies have reported that S-wave reflectors in the crust often represent crustal fluids (Aoki et al., 2016; Doi & Nishigami, 2007; Inamori et al., 2009; Kosuga, 2014; Matsumoto & Hasegawa, 1996).

Visual inspection of the seismic waveforms revealed that earthquakes occurring in Cluster N often have a distinct reflection phase in the waveforms recorded at station N.SUZH, which is located east of Cluster N. An example of this is shown in Figure 11. The particle motion in this phase was dominated by horizontal motion rather than particle motion upon direct arrival (Fig. S8), suggesting that this phase is an S-wave reflected from deeper than a direct wave. Although reflected phases were sometimes observed in other clusters and stations, they were not as clear as those observed at the N.SUZH station. Therefore, in this study, we estimated the reflection points using only the earthquakes in Cluster N (1200 events of M>1.5) and the N.SUZH station.

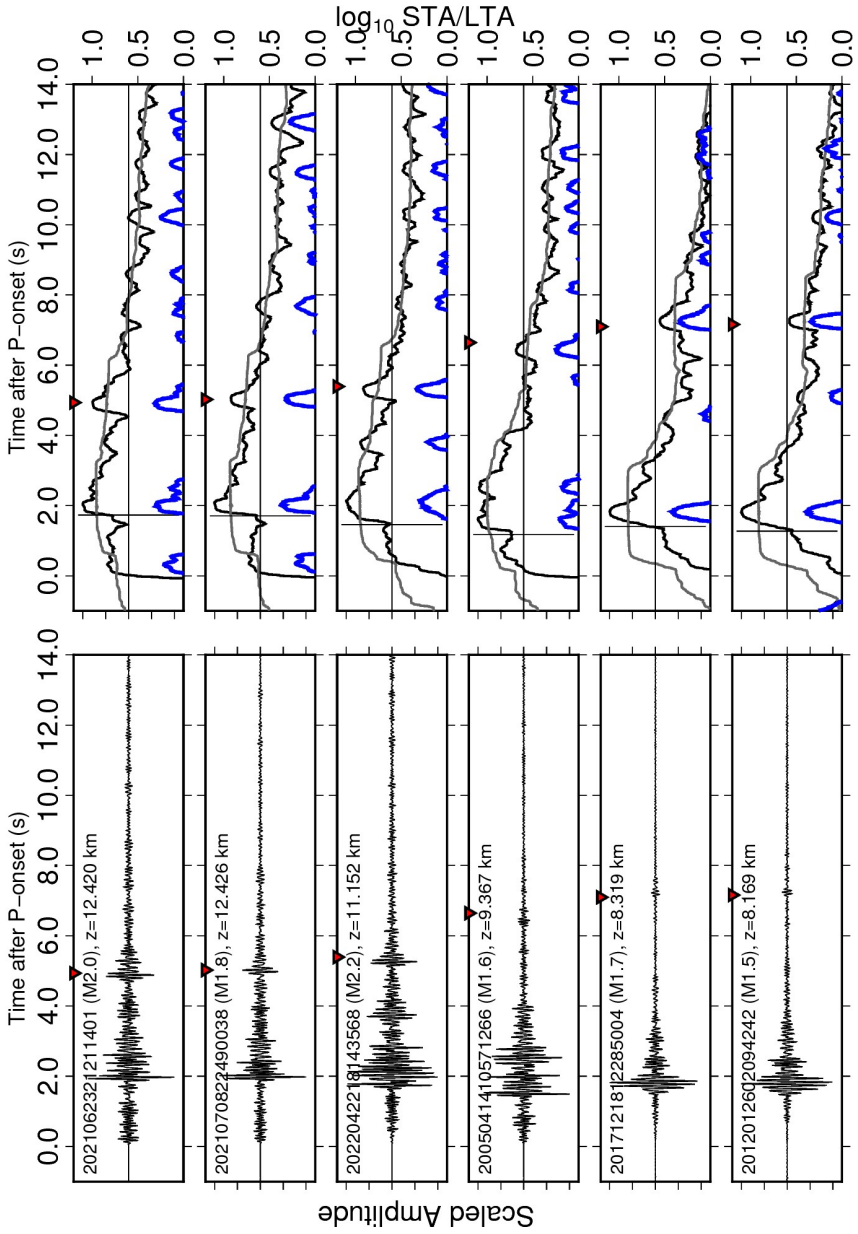

Figure 11. Example of reflected phases. The six figures on the left show observed waveforms (8–16 Hz) for six earthquakes. The six figures on the right show the logarithmic amplitudes of the two envelopes (black and gray) of the waveform on the left and the difference between them (blue). Black and gray lines are envelopes obtained based on short- and long-time averaged root mean square (RMS), respectively. The red triangle represents the timing at which the S×S wave would arrive when a reflection occurred at the best reflection point

(star) shown in Figure 12.

We used a back-projection method to search for the S-wave reflector location as described previously by Kosuga (2014). This method places grids around the source area and evaluates how well the observed seismic waveform amplitude can be explained when reflections occur in each grid. First, we squared the amplitude of the observed seismic waveform (8–16 Hz) and computed the log moving average over two different length time windows (0.33 s and 2.67 s) to obtain the envelope $\mathrm{ST}A_j(t)$ for the short time window and $\mathrm{LTA}_j(t)$ for the long window (Fig. 11). Here, subscript j denotes the j-th earthquake. The envelope calculation method was as described by Hiramatsu et al. (2000). The envelope ratio $R_j(t) = \frac{\mathrm{ST}A_j(t)}{\mathrm{LT}A_j(t)}$ was then calculated to emphasize the reflection phase, and its logarithm $r_j(t) = \log R_j(t)$ was used in subsequent analysis.

We calculated the time t_i required for the reflected wave to reach the station when a reflection occurred at each grid. In particular, we computed the time t_{i_1} required for the S-wave to reach the i-th grid from the earthquake hypocenter and the time t_{i_2} required for the S-wave to reach the station from the grid, and then obtained the sum $t_i = t_{i_1} + t_{i_2}$. We used the same 1-D velocity structure of Hasegawa et al. (1978) for hypocenter relocation. For each grid, we obtained the stacked amplitudes $A\left(x_i, y_i, z_i\right) = \sum_{j=1}^{n_{\mathrm{eq}}} r_j\left(t_i\right)$ for different earthquakes, where $n_{\mathrm{eq}} = 1204$ indicates the number of earthquakes. Grids with large values of $A(x_i, y_i, z_i)$ were regarded as candidate reflector locations. Note that using only a single earthquake and station does not provide a good constraint on the reflection location; therefore, we used multiple (>1200) earthquakes to constrain candidate reflection locations. The grid spacing was 0.001° horizontally and 0.2 km in depth, and data within 1.0 s of S-wave arrival were not used to prevent contamination of the stacked amplitude by direct S-waves. This indicates that we could not examine the grids near the earthquake hypocenters (Cluster N).

Figure 12 shows the distribution of the stacked amplitude $A(x_i, y_i, z_i)$ in the area around the reflector location. $A(x_i, y_i, z_i)$ had the maximum value south of the seismic Cluster N. A wide-area map for each depth is shown in Figure S9. Although a reflector may have a spatial extent within the region of large amplitude A, the present analysis method assumed that the reflection occurred at the same point; therefore, we focused on the point with the largest amplitude value. The reflector was located near the northern end of Cluster S near the deepest point (17 km) of this earthquake swarm and coincided with the location where this swarm began. This suggests that a fluid source exists near this point, and that the released fluids contribute to swarm initiation. In Figure 11, the arrival times of the reflected waves based on the best reflection point (t_i) explain the visible reflected phase well. The reflector location was estimated to be the same, even when we performed the same analysis by dividing the entire period into four parts (Fig. S10).

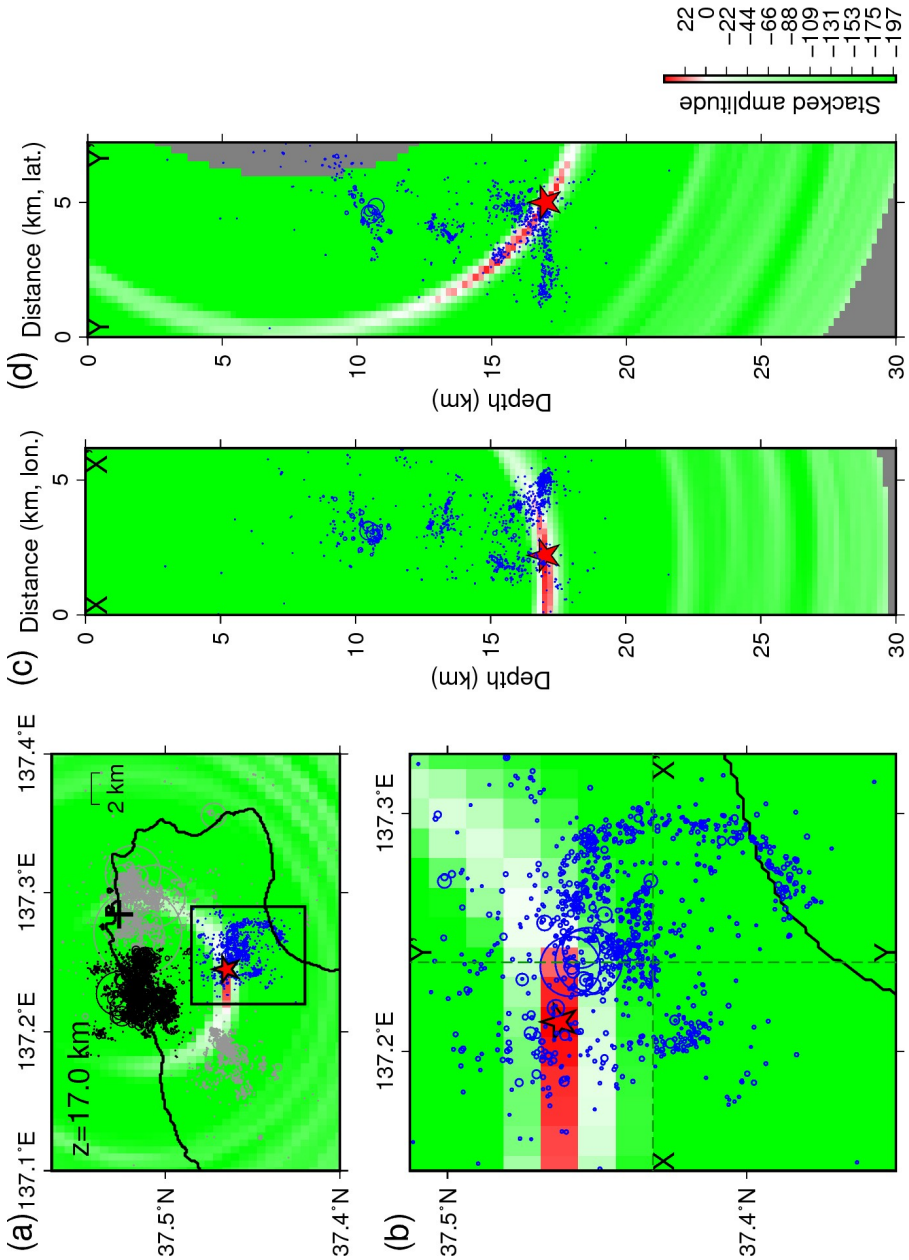

Figure 12. Comparison of the hypocenter distribution of Cluster S and the reflection point. (a)

The stacked envelope amplitude was calculated by back-projection. The color indicates the envelope amplitude that can be accounted for when S×S reflections occur at that location. Star indicates the maximum location. The grids

for which the number of available waveform data were less than half the total are shown in gray. Blue circles represent hypocenters in Cluster S, black circles represent Cluster N, and gray circles represent all other hypocenters. (b) Magnified view of the square area in (a) at a depth of 17.0 km. (c), (d) Two cross-sections shown in (b).

1. Discussion

The intense earthquake swarm in the northeastern Noto Peninsula became active on approximately December 1, 2020. Although earthquakes had occurred before this date, the seismicity increased sharply after this date (Fig. 1c). The earthquake swarm started in the deepest part of Cluster S and expanded in the order of Clusters W, N, and E. The details of the phenomenon in the intercluster region are not obvious. However, in Clusters W, N, and E, the earthquakes started at the deeper part and migrated to a shallower level (Fig. 6). This earthquake migration occurred via multiple plane structures (Fig. 7), suggesting that the current earthquake swarm occurred during the migration of crustal fluids from deep to shallow areas via multiple existing planes.

One essential question is where the fluids that generated the present earthquake swarm originated. Focusing on the area around the starting point of this swarm activity (Fig. 12b), we found that these locally deep earthquakes formed a characteristic ring-like distribution. An S-wave reflector was located in the immediate vicinity. This characteristic ring-like distribution was similar to the ring dike structure formed just above the magma chambers associated with caldera collapse (Johnson et al., 2002; Tomek et al., n.d.; T. Yoshida, 1984) and/or with magmatic intrusion in the middle crust (Johnson et al., 2002). Previous studies have reported the occurrence of earthquakes on such ring faults near known caldera structures (Mori & McKee, 1987; Sandanbata et al., 2021; Wilcock et al., 2016). The existence of a ring-like distribution of the hypocenters at 15–17-km depth indicates that the pre-existing ring dike was re-activated by fluids and/or that the ring dike was being formed or extended by an active intrusion of magma. In either case, the S-wave reflector may represent the upper edge of a magma reservoir, or a fluid concentration area released during magma solidification, and the released fluid may generate an earthquake swarm and migration. The solidified magma chamber could also be reactivated by a new intrusion.

Figures 13d and e show the S-wave structure from the seismic tomography by Nakajima & Hasegawa (2007). A low-velocity region of the S-wave was found in the lower part of the reflector and ring fault. Deep S-wave low-velocity regions similar to the present one are known in the lower crust beneath other calderas formed in the late Miocene, and many recent earthquake swarms have occurred there in Japan (Nakajima et al., 2006; Yoshida & Hasegawa, 2018; T. Yoshida et al., 2014). The S-wave low-velocity zone extending from the lower to middle crust of the deep Miocene caldera suggests the presence of a solidified deep magma reservoir and may indicate a deep-to-shallow upward pathway of fluids (Hasegawa et al., 2005). This supports the hypothesis that a fluid source exists

near the deepest part of Cluster S and that fluid movement from this source caused an intense earthquake swarm. Similarly, the resistivity structure suggests the existence of fluids deep in the crust in the western part of the region where the 2007 M6.9 earthquake occurred (Yoshimura et al., 2008). Hot springs are still distributed in the vicinity, and high helium isotope ratios (3He/4He) have also been observed in this area (Umeda et al., 2009).

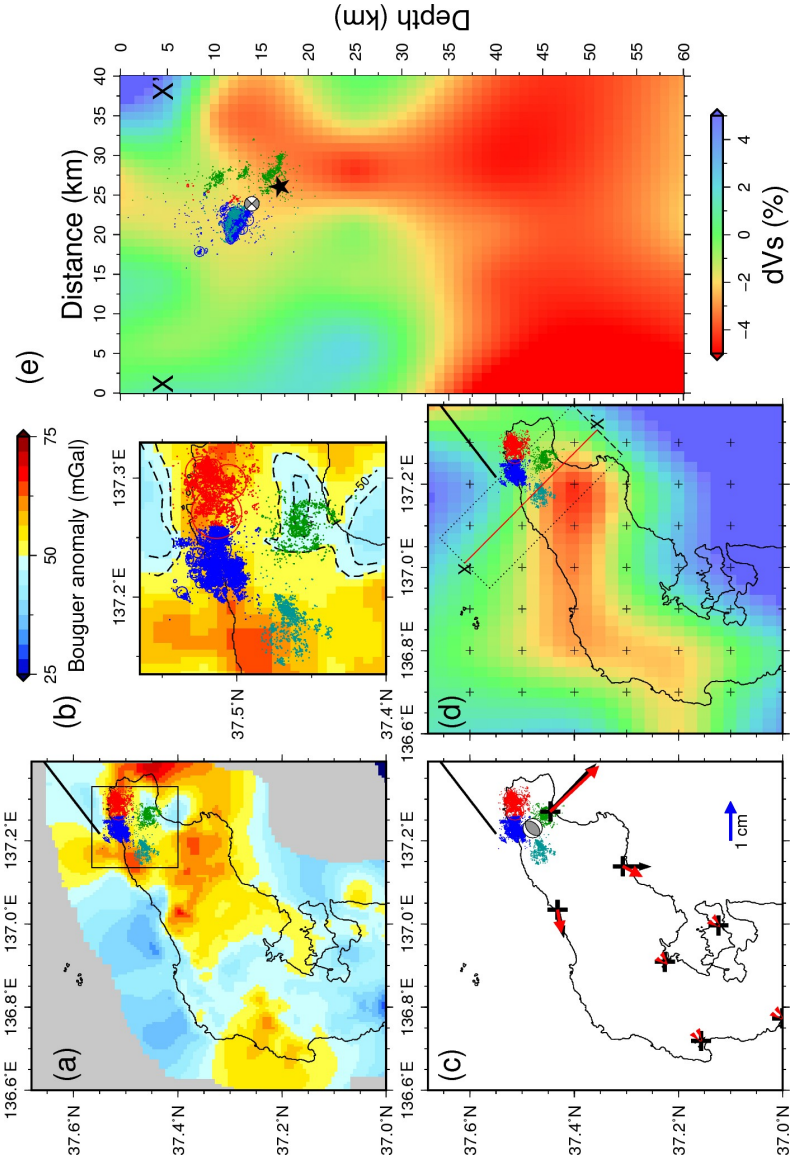

Figure 13. Comparison with crustal deformation, gravity anomalies, and seismic tomography results. (a) and (b) the Bouguer anomaly estimated by GSJ

(2013) are shown in color. The thick black line represents the Suzu-oki active fault segment (Inoue et al., 2010). The square in (a) represents the range in (b). (c) Crustal deformation. The black arrows represent displacement fields obtained by GEONET, and red ones represent the synthetic displacement fields based on the point source shown by the gray beach ball in (c) and (e). (d) and (e) Map (z = 25 km) and a cross-sectional view showing S-wave velocity estimated by Nakajima & Hasegawa (2007). Black star represents the locations of the seismic reflector detected in this study.

Currently, this area has no volcanic activity, with strata from the Oligocene to the Late Miocene distributed on the surface (Ozaki, 2010). However, during the Early to Middle Miocene (ca. 15–20 Ma) opening of the Sea of Japan, active felsic volcanism occurred in this area (Ozaki, 2010; Shimazu et al., 1993). The most recent volcanic activity in this area was rhyolitic volcanism in the middle Miocene (15.6 Ma) Awagura Formation. After that volcanic activity, oceanic sediments [Iida Formation (15.4–13.0 Ma) and Iizuka Formation (13–6.5 Ma)] overlie the Awagura Formation with glauconite sandstone in between and are thickly accumulated over the Cluster S area (Ozaki, 2010). It is possible that volcanic activity related to the Awagura Formation caused the Cluster S area to collapse rapidly during caldera formation, and thick marine strata were deposited there. Figures 13a and b show the Bouguer anomaly estimated by the Geological Survey of Japan (GSJ), AIST (National Institute of Advanced Industrial Science and Technology) assuming a crustal density of 2670 kg/m^3 (GSJ, 2013). A relatively high Bouguer anomaly characterizes the northeastern Noto Peninsula region. However, there was a locally pronounced low-gravity anomaly directly above Cluster S (green circles in Fig. 13b). This low-gravity anomaly may reflect a hidden caldera (Awagura Buried Caldera), which was previously unrecognized because it is covered by thick Middle-to-Late Miocene marine strata at the surface. This coincidence is consistent with the idea that a solidified magma chamber generated during volcanic activity in the Middle Miocene Awagura Formation exists deep in the vicinity of Cluster S while maintaining a high water content. Clusters other than Cluster S appear to be located in the periphery of the high-gravity anomalies surrounding the low-gravity anomaly area. These may have occurred using structures related to caldera formation, such as cone sheets (Phillips, 1974).

On the shallow side of Cluster S, a small number of earthquakes occurred before the activation of the present cluster of earthquakes. The seismic activity was also burst-like (Fig. 6), as is often observed in hydro-fracturing cases (Shapiro et al., 2006), suggesting the existence of extremely high pore pressure. It is possible that the fluid movement was not a one-time event and that other fluid sources may exist in the surrounding area. Even during the activation around 2018 at a depth of about 13 km, the earthquakes appear to be gradually moving shallower (t=-1300 to 0 days in Fig. S11).

Based on the proximity of the activated timing and the common characteristics of earthquake migration, it is likely that the same factors also contributed to

earthquake clusters other than Cluster S. However, there is a seismogenic gap between Cluster S and other clusters. The earthquakes in Clusters S, W, and N appear as a whole to be distributed near a single zone dipping approximately southeastward (Fig. 5). This may indicate that a southeast-dipping, highly permeable zone exists between Clusters S, W, and N, and fluid originating from the depth of cluster S may have used this zone to reach the other clusters. Cluster E was located shallower than this planar structure and may have been caused by fluid ascent using a different path.

In the northern clusters, most of the earthquakes occurred along ENE–WSW to NE–SW trending structures (Fig. 7), which is parallel to the trend of geological reverse faults and fold axes. Reactivation of normal faults as reverse or oblique slip faults is a common feature in the western part of the Noto Peninsula (Sato et al., 2007), which may indicate that the present reverse-fault earthquakes occurred at the deeper part of the Miocene listric normal fault. The length of the fault that caused the largest M5.4 earthquake appears to be 2- or 3-times larger than the rupture area, and the M5.4 and smaller earthquakes probably ruptured only a portion of this fault. There may be another large earthquake on the shallower high-dipping side of this fault. It is difficult for reverse fault earthquakes to occur on a high-angle fault plane, but they may be possible under extremely high pore pressures (Sibson, 1985).

Significant crustal deformation was observed during this earthquake swarm (Nishimura 2022); Figure 13c shows the displacement from December 1, 2020, to June 1, 2022, based on the GEONET F5 solutions with a distant station considered as the reference point (station ID:1158). Displacements of over 1 cm were observed near the source area, which was not explained solely by seismic activity. Significant crustal deformation was also observed during a large earthquake swarm in Matsushiro, Japan, in the 1960s and was thought to be the result of water eruption processes (Kisslinger, 1975; Sibson, 1996). Recent observational studies have suggested that fluid injection causes aseismic slip (Guglielmi et al., 2015) or fault opening based on geodetic data (Rossi et al., 2016; Yukutake et al., 2022) and seismicity (Barros et al., 2020; Hatch et al., 2020; Yoshida & Hasegawa, 2018). From realistic frictional properties, it is natural that pore pressure changes promote not only seismic but also aseismic slip (e.g., Yoshida et al., 2021). It is possible that aseismic deformation, such as an aseismic slip or fault opening, occurred in this seismic gap area.

We cannot constrain the origin of this aseismic deformation using the present data alone, as only three stations observed significant displacements. We checked whether the present idea of aseismic deformation in the seismic gap was consistent with the available data. We computed the synthetic displacements caused by an aseismic slip at the center of the seismic gap using the reflectivity code of Zhu & Rivera (2002). We assumed a point source of Mw 6.2 with a pure reverse fault consistent with the overall planar structure (strike and dip angles of 45°) at a depth of approximately 14.5 km. The results showed that this very simple source explained the observed displacements well

(Fig. 13c). To examine aseismic deformation during this earthquake swarm in detail, an analysis with more robust data is necessary (Nishimura et al., 2022).

Deep-source fluids play an essential role in the generation of crustal earthquakes in subduction zones. In particular, earthquakes occurring in volcanic regions are likely to be influenced by fluids related to magmatic activity that have dehydrated and ascended from the slab. Past or new magmatic activity may also supply fluid to the crust and generate earthquakes; however, it is not easy to find traces of magmatic activity from surface observations. The present results suggested that deep-source fluids originating from hidden magma-induced structures can generate earthquakes, even in areas where no volcanic activity has been observed at the surface for over 10 million years.

5. Conclusion

Intense earthquake swarms are occurring in the non-volcanic area northeast of the Noto Peninsula. This sequence exhibits a characteristic behavior similar to that of earthquake swarms in volcanic regions. The observed upward migration of earthquake hypocenters via multiple planes probably reflects fluid movement from deep to shallow depths. The S-wave reflectors near the swarm initiation point likely represent a fluid source. The deep ring-like distribution of hypocenters near the reflector suggests that the earthquake swarm was initiated by fluid outflow from a ring dike formed over a magma reservoir associated with past caldera collapse and/or current magma intrusion. The remarkable crustal deformation observed during this earthquake swarm is likely related to the fluid supply that contributed to the intense earthquake swarm. The present results suggest that hidden magma-induced structures and fluids can generate earthquakes even in areas where no volcanic activity has been observed for over 10 million years.

Acknowledgements

The discussion with Naoshi Hirata and Takuya Nishimura on the details of this earthquake swarm was beneficial in improving the discussion. We used the results of Bouguer anomaly data from the Geological Survey of Japan (GSJ), National Institute of Advanced Industrial Science and Technology (AIST). The figures were created using GMT (Wessel and Smith 1998). This study was supported by JSPS KAKENHI (Grant Number JP 20K14569 and JP 20K05394).

Data availability

This study used hypocenter and S-wave arrival time data reported in the JMA unified catalog. Seismograms were collected and stored by the JMA, national universities, and NIED (http://www.hinet.bosai.go.jp/?LANG=en). The seismograms used in this study were collected and stored by JMA, national universities, and NIED (Hi-net: https://doi.org/10.17598/NIED.0003; F-net: https://doi.org/10.17598/NIED.0005; and KiK-net: https://doi.org/10.17598/NIED.0004). Waveform data were obtained from the NIED Hi-net website (http://www.hinet.bosai.go.jp/?LANG=en). The gravity database by GSJ (2013) was

used for the Bouguer anomaly (https://www.gsj.jp/Map/JP/geophysics3.html).

References

Amezawa, Y., Maeda, T., & Kosuga, M. (2021). Migration diffusivity as a controlling factor in the duration of earthquake swarms. *Earth, Planets and Space*, *73*(1), 148. https://doi.org/10.1186/s40623-021-01480-7

Aoki, S., Iio, Y., Katao, H., Miura, T., Yoneda, I., & Sawada, M. (2016). Three-dimensional distribution of S wave reflectors in the northern Kinki district, southwestern Japan. *Earth, Planets and Space*, *68*(1), 107. https://doi.org/10.1186/s40623-016-0468-3

Aso, N., Ohta, K., & Ide, S. (2011). Volcanic-like low-frequency earthquakes beneath Osaka Bay in the absence of a volcano. *Geophysical Research Letters*, *38*(8), n/a-n/a. https://doi.org/10.1029/2011gl046935

Bachmann, C. E., Wiemer, S., Goertz-Allmann, B. P., & Woessner, J. (2012). Influence of pore-pressure on the event-size distribution of induced earthquakes. *Geophysical Research Letters*, *39*(9), n/a-n/a. https://doi.org/10.1029/2012gl051480

Barros, L. D., Cappa, F., Deschamps, A., & Dublanchet, P. (2020). Imbricated Aseismic Slip and Fluid Diffusion Drive a Seismic Swarm in The Corinth Gulf, Greece. *Geophysical Research Letters*, e2020GL087142. https://doi.org/10.1029/2020gl087142

Cox, S. F. Injection-Driven Swarm Seismicity and Permeability Enhancement: Implications for the Dynamics of Hydrothermal Ore Systems in High Fluid-Flux, Overpressured Faulting Regimes—An Invited Paper. *Econ Geol* **111**, 559–587 (2016).

Doi, I., & Nishigami, K. (2007). Three-dimensional distributions of S wave reflectors in the source region of the 2000 Western Tottori Earthquake. *Geophysical Research Letters*, *34*(20). https://doi.org/10.1029/2007gl031169

Fischer, T., Horálek, J., Hrubcová, P., Vavryčuk, V., Bräuer, K., & Kämpf, H. (2014). Intra-continental earthquake swarms in West-Bohemia and Vogtland: A review. *Tectonophysics*, *611*, 1–27. https://doi.org/10.1016/j.tecto.2013.11.001

GSJ. (2013). Gravity database of Japan DVD Edition, https://www.gsj.jp/Map/JP/geophysics3.html.

Guglielmi, Y., Cappa, F., Avouac, J.-P., Henry, P., & Elsworth, D. (2015). Seismicity triggered by fluid injection–induced aseismic slip. *Science*, *348*(6240), 1224–1226. https://doi.org/10.1126/science.aab0476

Hartzell, S. H., & Heaton, T. H. (1983). Inversion of strong ground motion and teleseismic waveform data for the fault rupture history of the 1979 Imperial Valley, California, earthquake. *Bulletin of the Seismological Society of America*.

Hasegawa, A., Umino, N., & Takagi, A. (1978). Double-planed structure of the deep seismic zone in the northeastern Japan arc. *Tectonophysics*, *47*(1–2),

43–58. https://doi.org/10.1016/0040-1951(78)90150-6

Hasegawa, A., & Yamamoto, A. (1994). Deep, low-frequency microearthquakes in or around seismic low-velocity zones beneath active volcanoes in northeastern Japan. *Tectonophysics*, *233*(3–4), 233–252. https://doi.org/10.1016/0040-1951(94)90243-7

Hasegawa, A., Nakajima, J., Umino, N., & Miura, S. (2005). Deep structure of the northeastern Japan arc and its implications for crustal deformation and shallow seismic activity. *Tectonophysics*, *403*(1–4), 59–75. https://doi.org/10.1016/j.tecto.2005.03.018

Haskell, N. A. (1964). TOTAL ENERGY AND ENERGY SPECTRAL DENSITY OF ELASTIC WAVE RADIATION FROM PROPAGATING FAULTS. *Bulletin of the Seismological Society of America.*

Hatch, R. L., Abercrombie, R. E., Ruhl, C. J., & Smith, K. D. (2020). Evidence of Aseismic and Fluid-Driven Processes in a Small Complex Seismic Swarm Near Virginia City, Nevada. *Geophysical Research Letters*, *47*(4). https://doi.org/10.1029/2019gl085477

Hiramatsu, Y., Hayashi, N., Furumoto, M., & Katao, H. (2000). Temporal changes in coda Q −1 and b value due to the static stress change associated with the 1995 Hyogo-ken Nanbu earthquake. *Journal of Geophysical Research: Solid Earth*, *105*(B3), 6141–6151. https://doi.org/10.1029/1999jb900432

Hori, S., Umino, N., Kono, T., & Hasegawa, A. (2004). Distinct S-wave Reflectors (Bright Spots) Extensively Distributed in the Crust and Upper Mantle beneath the Northeastern Japan Arc. *Zisin 2*, *56*(4), 435–446. https://doi.org/10.4294/zisin1948.56.4_435

Inamori, T., Horiuchi, S., & Hasegawa, A. (2009). Location of Mid-Crustal Reflectors by a Reflection Method Using Aftershock Waveform Data in the Focal Area of the 1984 Western Nagano Prefecture Earthquake. *Journal of Physics of the Earth*, *40*(2), 379–393. https://doi.org/10.4294/jpe1952.40.379

Inoue, T. and Okamura, Y. (2010), Explanatory notes of 1:200,000 marine geological map around the northern part of Noto Peninsula, Seamless geoinformation of Coastal zone "Northern Coastal Zone of Noto Peninsula" (DVD), Digital Geoscience Map S-1, Geological Survey of Japan, AIST.

Iwamori, H. (1998). Transportation of H2O and melting in subduction zones. *Earth and Planetary Science Letters*, *160*(1–2), 65–80. https://doi.org/10.1016/s0012-821x(98)00080-6

Johnson, S. E., Schmidt, K. L., & Tate, M. C. (2002). Ring complexes in the Peninsular Ranges Batholith, Mexico and the USA: magma plumbing systems in the middle and upper crust. *Lithos*, *61*(3–4), 187–208. https://doi.org/10.1016/s0024-4937(02)00079-8

Kanamori, H., Ross, Z. E., & Rivera, L. (2020). Estimation of radiated energy

using the KiK-net downhole records—old method for modern data. *Geophysical Journal International*, *221*(2), 1029–1042. https://doi.org/10.1093/gji/ggaa040

Kato, A., Sakai, S., Iidaka, T., Iwasaki, T., Kurashimo, E., Igarashi, T., et al. (2008). Three-dimensional velocity structure in the source region of the Noto Hanto Earthquake in 2007 imaged by a dense seismic observation. *Earth, Planets and Space*, *60*(2), 105–110. https://doi.org/10.1186/bf03352769

Kikuchi, M., & Kanamori, H. (1982). Inversion of complex body waves. *Bulletin of the Selsmologmal Society of America*.

Kisslinger, C. Processes during the Matsushiro, Japan, Earthquake Swarm as Revealed by Leveling, Gravity, and Spring-Flow Observations. *Geology* **3**, 57–62 (1975).

Kosuga, M. (2014). Seismic activity near the Moriyoshi-zan volcano in Akita Prefecture, northeastern Japan: implications for geofluid migration and a mid-crustal geofluid reservoir. *Earth, Planets and Space*, *66*(1), 77. https://doi.org/10.1186/1880-5981-66-77

Kusuda, C., Iwamori, H., Nakamura, H., Kazahaya, K., & Morikawa, N. (2014). Arima hot spring waters as a deep-seated brine from subducting slab. *Earth, Planets and Space*, *66*(1), 119. https://doi.org/10.1186/1880-5981-66-119

Ligorria, J., & Ammon, C. (1999). Iterative deconvolution and receiver-function estimation. *Bulletin of the Seismological*.

Matsumoto, S., & Hasegawa, A. (1996). Distinct S wave reflector in the mid-crust beneath Nikko-Shirane volcano in the northeastern Japan arc. *Journal of Geophysical Research: Solid Earth*, *101*(B2), 3067–3083. https://doi.org/10.1029/95jb02883

Matsumoto, Y., Yoshida, K., Matsuzawa, T., & Hasegawa, A. (2021). Fault-valve behavior estimated from intensive foreshocks and aftershocks of the 2017 M 5.3 Kagoshima Bay earthquake sequence, Kyushu, southern Japan. *Journal of Geophysical Research: Solid Earth*. https://doi.org/10.1029/2020jb020278

Mcbirney, A. R. (1969). The Earth's Crust and Upper Mantle. *Geophysical Monograph Series*, 501–507. https://doi.org/10.1029/gm013p0501

Mori, J., & McKee, C. (1987). Outward-Dipping Ring-Fault Structure at Rabaul Caldera as Shown by Earthquake Locations. *Science*, *235*(4785), 193–195. https://doi.org/10.1126/science.235.4785.193

Morikawa, N., Kazahaya, K., Takahashi, M., Inamura, A., Takahashi, H. A., Yasuhara, M., et al. (2016). Widespread distribution of ascending fluids transporting mantle helium in the fore-arc region and their upwelling processes: Noble gas and major element composition of deep groundwater in the Kii Peninsula, southwest Japan. *Geochimica et Cosmochimica Acta*, *182*, 173–196. https://doi.org/10.1016/j.gca.2016.03.017

Mukuhira, Y., Fehler, M. C., Ito, T., Asanuma, H., & Häring, M. O. (2021). Injection induced seismicity size distribution dependent on shear stress. *Geophysical Research Letters*. https://doi.org/10.1029/2020gl090934

Nakajima, J., & Hasegawa, A. (2007). Deep crustal structure along the Niigata-Kobe Tectonic Zone, Japan: Its origin and segmentation. *Earth, Planets and Space*, *59*(2), e5–e8. https://doi.org/10.1186/bf03352677

Nakajima, J., Hasegawa, A., Horiuchi, S., Yoshimoto, K., Yoshida, T., & Umino, N. (2006). Crustal heterogeneity around the Nagamachi-Rifu fault, northeastern Japan, as inferred from travel-time tomography. *Earth, Planets and Space*, *58*(7), 843–853. https://doi.org/10.1186/bf03351989

NIED (2019aa). NIED Hi-net, National Research Institute for Earth Science and Disaster Resilience,. https://doi.org/10.17598/nied.0003

NIED (2019b). NIED F-net, National Research Institute for Earth Science and Disaster Resilience. https://doi.org/10.17598/nied.0005

NIED (2019c). NIED K-NET, KiK-net, National Research Institute for Earth Science and Disaster Resilience. https://doi.org/10.17598/nied.0004

Okada, T., Matsuzawa, T., Umino, N., Yoshida, K., Hasegawa, A., Takahashi, H., et al. (2015). Hypocenter migration and crustal seismic velocity distribution observed for the inland earthquake swarms induced by the 2011 Tohoku-Oki earthquake in NE Japan: implications for crustal fluid distribution and crustal permeability. *Geofluids*, *15*(1–2), 293–309. https://doi.org/10.1111/gfl.12112

Ozaki, M. (2010). 1:200,000 Geological map of the northern part of Noto Peninsula. In *S-1. Seamless geoinformation of coastal zone "Northern coastal zone of Noto Peninsula"* (p. P013).

Parotidis, M., Rothert, E., & Shapiro, S. A. (2003). Pore-pressure diffusion: A possible triggering mechanism for the earthquake swarms 2000 in Vogtland/NW-Bohemia, central Europe. *Geophysical Research Letters*, *30*(20), n/a-n/a. https://doi.org/10.1029/2003gl018110

Phillips, W. J. (1974). The dynamic emplacement of cone sheets. *Tectonophysics*, *24*(1–2), 69–84. https://doi.org/10.1016/0040-1951(74)90130-9

Ross, Z. E., Kanamori, H., Hauksson, E., & Aso, N. (2018). Dissipative Intraplate Faulting During the 2016 Mw 6.2 Tottori, Japan Earthquake. *Journal of Geophysical Research: Solid Earth*, *123*(2), 1631–1642. https://doi.org/10.1002/2017jb015077

Rossi, G., Zuliani, D., & Fabris, P. (2016). Long-term GNSS measurements from the northern Adria microplate reveal fault-induced fluid mobilization. *Tectonophysics*, *690*, 142–159. https://doi.org/10.1016/j.tecto.2016.04.031

Sandanbata, O., Kanamori, H., Rivera, L., Zhan, Z., Watada, S., & Satake, K. (2021). Moment Tensors of Ring-Faulting at Active Volcanoes: Insights into Vertical-CLVD Earthquakes at the Sierra Negra Caldera, Galápagos Islands.

Journal of Geophysical Research: Solid Earth, *126*(6). https://doi.org/10.1029/2021jb021693

Scholz, C H. (1968). Microfracturing and the inelastic deformation of rock in compression. *Journal of Geophysical Research*, *73*(4), 1417–1432. https://doi.org/10.1029/jb073i004p01417

Scholz, C H. (2015). On the stress dependence of the earthquake b value. *Geophysical Research Letters*, *42*(5), 1399–1402. https://doi.org/10.1002/2014gl062863

Shapiro, S. A., Huenges, E., & Borm, G. (1997). Estimating the crust permeability from fluid-injection-induced seismic emission at the KTB site. *Geophysical Journal International*, *131*(2), F15–F18. https://doi.org/10.1111/j.1365-246x.1997.tb01215.x

Shapiro, S. A., Dinske, C., & Rothert, E. (2006). Hydraulic-fracturing controlled dynamics of microseismic clouds. *Geophysical Research Letters*, *33*(14). https://doi.org/10.1029/2006gl026365

Shelly, D. R., & Hill, D. P. (2011). Migrating swarms of brittle-failure earthquakes in the lower crust beneath Mammoth Mountain, California. *Geophysical Research Letters*, *38*(20), n/a-n/a. https://doi.org/10.1029/2011gl049336

Shelly, D. R., Hill, D. P., Massin, F., Farrell, J., Smith, R. B., & Taira, T. (2013). A fluid-driven earthquake swarm on the margin of the Yellowstone caldera. *Journal of Geophysical Research: Solid Earth*, *118*(9), 4872–4886. https://doi.org/10.1002/jgrb.50362

Shi, Y., & Bolt, B. A. (1982). The standard error of the magnitude-frequency b value. *Bulletin of the Seismological Society of America*, *72*(5), 1677–1687. https://doi.org/10.1785/bssa0720051677

Shimazu, M., Kagami, H., Kawano, Y., & Yamamoto, G. (1993). Geochemistry of Early-Middle Miocene volcanic rocks in the backarc region of Japan: Sado, Noto and Tadami areas. *The Journal of the Geological Society of Japan*, *99*(10), 799–811. https://doi.org/10.5575/geosoc.99.799

Sibson, R. H. (1985). A note on fault reactivation. *Journal of Structural Geology*, *7*(6), 751–754. https://doi.org/10.1016/0191-8141(85)90150-6

Sibson, R. H. (1996). Structural permeability of fluid-driven fault-fracture meshes. *Journal of Structural Geology*, *18*(8), 1031–1042. https://doi.org/10.1016/0191-8141(96)00032-6

Taira, T., Yomogida, K., Kuwahara, Y., Imanishi, K., & Ito, H. (2007). Imaging of crustal heterogeneous structures using a slowness-weighted back-projection with effects of scattering modes: 2. Application to the Nagamachi-Rifu fault, Japan, area. *Journal of Geophysical Research: Solid Earth (1978–2012)*, *112*(B6). https://doi.org/10.1029/2006jb004382

Tatsumi, Y., Sakuyama, M., Fukuyama, H., & Kushiro, I. (1983). Generation of arc basalt magmas and thermal structure of the mantle wedge in subduction zones. *Journal of Geophysical Research: Solid Earth*, *88*(B7), 5815–5825. https://doi.org/10.1029/jb088ib07p05815

Terakawa, T., Hashimoto, C., & Matsu'ura, M. (2013). Changes in seismic activity following the 2011 Tohoku-oki earthquake: Effects of pore fluid pressure. *Earth and Planetary Science Letters*, *365*, 17–24. https://doi.org/10.1016/j.epsl.2013.01.017

Tomek, F., Žák, J., Svojtka, M., Finger, F., & Waitzinger, M. (n.d.). Emplacement dynamics of syn-collapse ring dikes: An example from the Altenberg-Teplice caldera, Bohemian Massif. *GSA Bulletin*, *131*(5–6), 997–1016. https://doi.org/10.1130/b35019.1

Umeda, K., Ninomiya, A., & Negi, T. (2009). Heat source for an amagmatic hydrothermal system, Noto Peninsula, Central Japan. *Journal of Geophysical Research: Solid Earth*, *114*(B1). https://doi.org/10.1029/2008jb005812

Umino, N., Ujikawa, H., Hori, S., & Hasegawa, A. (2002). Distinct S-wave reflectors (bright spots) detected beneath the Nagamachi-Rifu fault, NE Japan. *Earth, Planets and Space*, *54*(11), 1021–1026. https://doi.org/10.1186/bf03353295

Usami. (2003). *A catalogue of disastrous earthquakes in Japan (updated ed.)*. University of Tokyo Press.

Vassiliou, M. & Kanamori, H. The energy release in earthquakes. the Seismological Society of (1982).

Yoshida, K., & Hasegawa, A. (2018a). Hypocenter Migration and Seismicity Pattern Change in the Yamagata-Fukushima Border, NE Japan, Caused by Fluid Movement and Pore Pressure Variation. *Journal of Geophysical Research: Solid Earth*, *123*(6), 5000–5017. https://doi.org/10.1029/2018jb015468

Yoshida, K., & Hasegawa, A. (2018b). Sendai-Okura earthquake swarm induced by the 2011 Tohoku-Oki earthquake in the stress shadow of NE Japan: Detailed fault structure and hypocenter migration. *Tectonophysics*. https://doi.org/10.1016/j.tecto.2017.12.031

Yoshida, K., Hasegawa, A., Okada, T., Takahashi, H., Kosuga, M., Iwasaki, T., et al. (2014). Pore pressure distribution in the focal region of the 2008 M7.2 Iwate-Miyagi Nairiku earthquake. *Earth, Planets and Space*, *66*(1), 59. https://doi.org/10.1186/1880-5981-66-59

Yoshida, K., Hasegawa, A., & Yoshida, T. (2016). Temporal variation of frictional strength in an earthquake swarm in NE Japan caused by fluid migration. *Journal of Geophysical Research: Solid Earth*, *121*(8), 5953–5965. https://doi.org/10.1002/2016jb013022

Yoshida, K., Saito, T., Urata, Y., Asano, Y., & Hasegawa, A. (2017). Temporal

Changes in Stress Drop, Frictional Strength, and Earthquake Size Distribution in the 2011 Yamagata-Fukushima, NE Japan, Earthquake Swarm, Caused by Fluid Migration. *Journal of Geophysical Research: Solid Earth*, *122*(12), 10,379-10,397. https://doi.org/10.1002/2017jb014334

Yoshida, K., Hasegawa, A., Yoshida, T., & Matsuzawa, T. (2019). Heterogeneities in Stress and Strength in Tohoku and Its Relationship with Earthquake Sequences Triggered by the 2011 M9 Tohoku-Oki Earthquake. *Pure and Applied Geophysics*, *176*(3), 1–21. https://doi.org/10.1007/s00024-018-2073-9

Yoshida, K., Taira, T., Matsumoto, Y., Saito, T., Emoto, K., & Matsuzawa, T. (2020). Stress Release Process Along an Intraplate Fault Analogous to the Plate Boundary: A Case Study of the 2017 M5.2 Akita-Daisen Earthquake, NE Japan. *Journal of Geophysical Research: Solid Earth*, *125*(5). https://doi.org/10.1029/2020jb019527

Yoshida, K., Noda, H., Nakatani, M. & Shibazaki, B. (2021). Backward earthquake ruptures far ahead of fluid invasion: Insights from dynamic earthquake-sequence simulations. *Tectonophysics,* 229038. doi:10.1016/j.tecto.2021.229038.

Yoshida, K., Matsuzawa, T., & Uchida, N. (2022). The 2021 Mw7.0 and Mw6.7 Miyagi-Oki earthquakes nucleated in a deep seismic/aseismic transition zone Possible effects of transient instability due to the 2011 Tohoku earthquake. *Journal of Geophysical Research: Solid Earth.* https://doi.org/10.1029/2022jb024887

Yoshida, T. (1984). Tertiary Ishizuchi Cauldron, southwestern Japan Arc: Formation by ring fracture subsidence. *Journal of Geophysical Research: Solid Earth*, *89*(B10), 8502–8510. https://doi.org/10.1029/jb089ib10p08502

Yoshida, T., Kimura, J.-I., Yamada, R., Acocella, V., Sato, H., Zhao, D., et al. (2014). Evolution of late Cenozoic magmatism and the crust–mantle structure in the NE Japan Arc. *Geological Society, London, Special Publications*, *385*(1), 335–387. https://doi.org/10.1144/sp385.15

Yoshikawa, T. *et al.* Geology of the Suzumisaki, Noto-iida and Horyuzan district. in *Geological Sheet Map at 1,50,000, Geological Survey of Japan* 76 pp. (2002).

Yoshimura, R., Oshiman, N., Uyeshima, M., Ogawa, Y., Mishina, M., Toh, H., et al. (2008). Magnetotelluric observations around the focal region of the 2007 Noto Hanto Earthquake (Mj 6.9), Central Japan. *Earth, Planets and Space*, *60*(2), 117–122. https://doi.org/10.1186/bf03352771

Yukutake, Y., Yoshida, K., & Honda, R. (2022). Interaction between aseismic slip and fluid invasion in earthquake swarms revealed by dense geodetic and seismic observations. *Journal of Geophysical Research: Solid Earth.* https://doi.org/10.1029/2021jb022933

Yukutake, Y., Tanada, T., Honda, R., Harada, M., Ito, H., & Yoshida, A. (2010). Fine fracture structures in the geothermal region of Hakone volcano, revealed

by well-resolved earthquake hypocenters and focal mechanisms. *Tectonophysics*, *489*(1–4), 104–118. https://doi.org/10.1016/j.tecto.2010.04.012

Waldhauser, F., & Ellsworth, W. L. (2000). A Double-Difference Earthquake Location Algorithm: Method and Application to the Northern Hayward Fault, California. *Bulletin of the Seismological Society of America*, *90*(6), 1353–1368. https://doi.org/10.1785/0120000006

Wilcock, W. S. D., Tolstoy, M., Waldhauser, F., Garcia, C., Tan, Y. J., Bohnenstiehl, D. R., et al. (2016). Seismic constraints on caldera dynamics from the 2015 Axial Seamount eruption. *Science*, *354*(6318), 1395–1399. https://doi.org/10.1126/science.aah5563

Zhu, L., & Rivera, L. A. (2002). A note on the dynamic and static displacements from a point source in multilayered media. *Geophysical Journal International*, *148*(3), 619–627. https://doi.org/10.1046/j.1365-246x.2002.01610.x